living ECs exposed to the physiological range of FSS by confocal microscopy and the measurement of the intracellular strain field together with the application of image processing and the finite element method (FEM).[18] They stained cytoplasmic domain and nuclei of living ECs with fluorescent dyes, respectively. The cells were cultured in parallel-plate flow chamber and the flow rate was controlled by a syringe pump. The scanning line of laser microscope was set to be parallel to the direction of flow crossing the vicinity of the center of the nucleus and containing two to four ECs in one frame. A personal computer with a customized program was used to synchronize the pushing motion of the syringe pump and the trigger signal for image acquisition by the microscope for a temporally well-coordinated measurement. To obtain the intracellular displacement field, an image correlation analysis was carried out between the undeformed and deformed images. The obtained lateral images of endothelial cells exposed to shear stress and the strain distribution in the cell calculated from the displacement field by FEM are shown in Fig. 1. The dynamic image during deformation under shear stress exposure can be found at the journal homepage: www.elsevier.com/locate/ybbrc.

Another technique is FRET (fluorescence resonance energy transfer) imaging to visualize the spatiotemporal activations of signaling proteins in a cell such as Rho family GTPase. Various kinds of FRET probes have been developed. For example, Raichu (Ras and interacting chimeric unit)-Rac1 and -RhoA are typical to visualize Rac1 and RhoA in living cells.[72,73]

Microbead Techniques

Although it remains unclear which molecule or cellular component is the primary mechanosensor, one of the major candidates is focal adhesions (FAs) consisting of integrins and associated molecules. Since FAs provide the mechanical linkage between the extracellular matrix and cytoskeletons, forces would be directly exerted on FAs when cells are exposed to external forces. Recent reports have shown that p130CAS[85] and talin[18] in FAs serve as primary mechanosensors, which trigger signal transduction cascades leading to alteration in cellular functions such as proliferation[86] and gene expression.[28] In addition, FAs may adapt to their mechanical environment by changing their structures and connections to cytoskeletons, and have an important role in mechanically-induced morphological and cytoskeletal remodeling of ECs. Previous studies using micro-manipulation techniques reported the accumulation of FA-associated molecules[30] and actin[20,38] when forces were applied to FAs, and local stiffening of cells[63] was induced by continuous or cyclic forces.

One of the typical methods of applying localized mechanical force is the use of microbeads. Glass and magnetic microbeads coated with a protein or a polypeptide are used to adhere to FAs.[34,94,99] Wang and Suo[99] reported that stress fibers have a role in force transmission. They applied mechanical stress at the apical side using magnetic bead technique, and then observed deformation at the basal side under low and high prestress, the tension acting in the cell. They
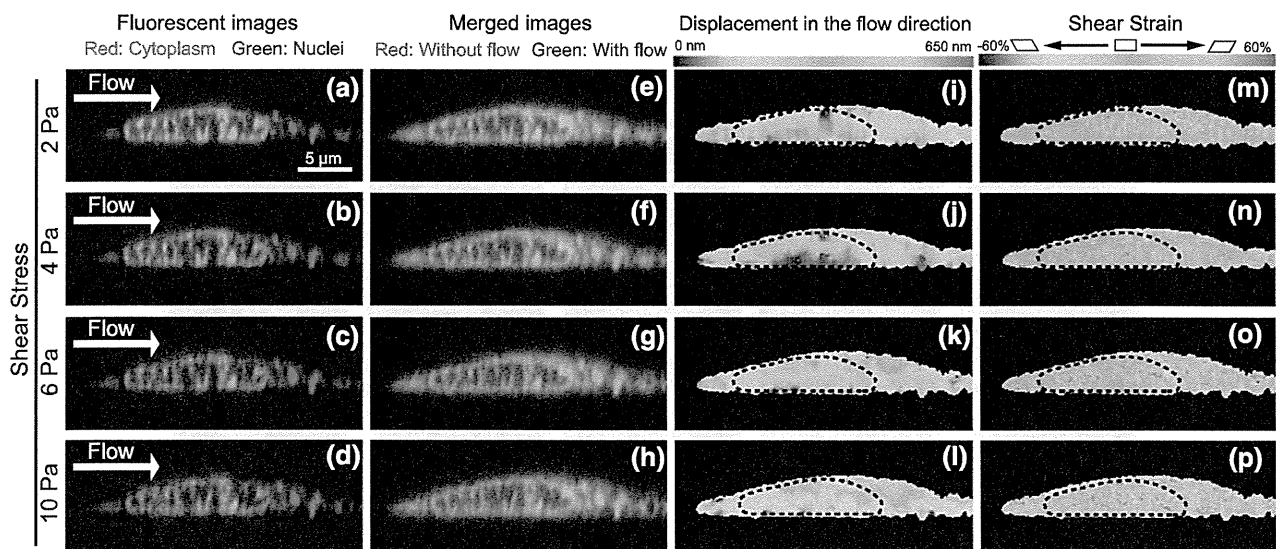

FIGURE 1. Lateral images of HUVECs exposed to FSSs of 2 (a, e, i, m), 4 (b, f, j, n), 6 (c, g, k, o), and 10 Pa (d, h, l, p). (a–d) Fluorescent images of nuclei (green) and cytoplasm (red) of HUVECs under given FSS. (e–h) Merged images of HUVECs under static (red) and flow (green) conditions. Disagreement of green and red colors indicates the displacement due to the flow. (i–l) Contour mappings of displacement in the flow direction. (m–p) Contour mappings of shear strain analyzed using FEM. The dextral and sinistral shear strains are indicated by warm and cold colors, respectively.

obtained basal deformation map at low prestress which led to localized displacement. However, at high prestress, mechanical stress was transmitted over a long distance. Another example is shown by Hayakawa et al.[34] by introducing a glass microbead to the cell surface. Stress fibers were developed to connect the apical FAs to the basal ones. When they moved the bead with glass micropipette by 4 μm, they observed the movement of small fluorescent beads with diameter of 50 nm embedded in the substrate gel. However, only very small displacement of beads was observed in cytochalasin-D treated cells. This observation has further supported that mechanical force transmits from the apical FAs to the basal ones.

Microtechnologies for Cell Mechanics

Recently, some developed micro-fabricated technologies have greatly enabled the study of cell mechanics and mechanobiology and in elucidating how they can regulate important biological processes such as cell adhesion, migration, spreading, and differentiation.

Microcontact Printing

Microcontact printing provides a simple way of producing patterns on substrates for altering and regulating cell shape, spreading and migration. One example is the use of microcontact printing to produce fibronectin patterns of varying sizes to demonstrate that the shape and spreading area of human mesenchymal stem cells (hMSCs) can regulate the differentiation of stem cells into specific lineages. Here, hMSCs seeded on small patterns of fibronectin (about

1024 μm^2) tended to differentiate into adipocytes (fat cells) while those seeded on large fibronectin patterns (about 10,000 μm^2) tended to differentiate into osteocytes (bone cells).[64] Other examples include the use of various other microcontact printed geometrical patterns (e.g., rectangle with different aspect ratios or pentagons with varying curvature of the edges) to show that the patterns that induce the increase of intracellular actomyosin tension regulate the differentiation behavior of MSCs.[44]

Microcontact printed pattern of fibronectin is also another simple way of regulating cell shape and influencing the cell division axis (Fig. 2). This axis along which a cell divides determines the position and fate of the daughter cells. In fact, the spatial distribution of extracellular matrix (ECM) was found to determine cortical actin dynamics which in turn regulate the axis of cell division.[91,92] Hence, it is important to understand how biomechanical cues imposed by the ECM proteins regulate cell division.

Cell migration is known to be influenced not only by chemical but also mechanical cues presented in their microenvironment including topography, geometrical constraints, and ECM protein distribution patterns. Micro-fabrication techniques have enabled us to systematically alter these mechanical cues to study how these factors can regulate cell migration. One example is the use of micro-patterned substrates to demonstrate that the migration of cells on very narrow patterns (one-dimensional or 1D migration) is faster than that on two-dimensional or 2D surfaces. A contributing reason is that the migration on narrow channels is much more dependent on myosin II than that of 2D migration.[23]
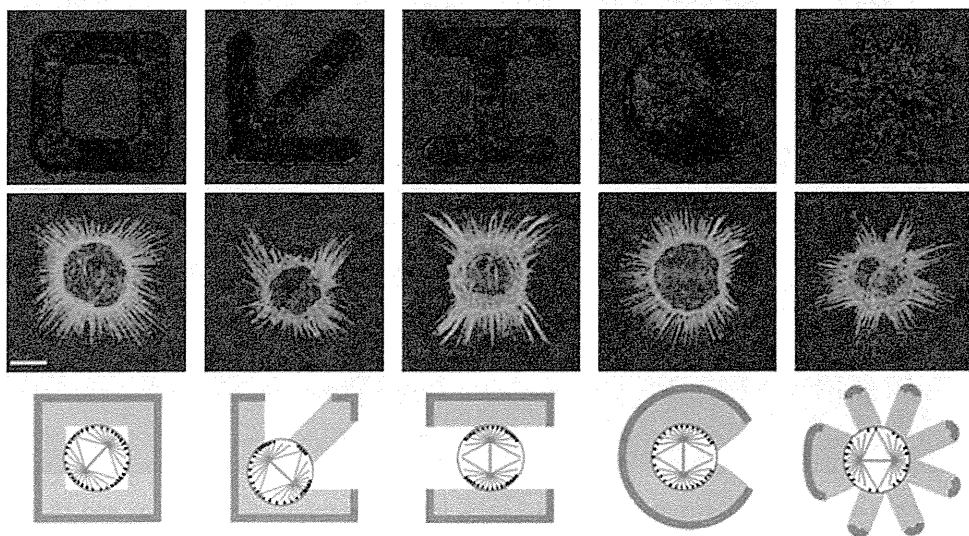

FIGURE 2. Demonstration of how various ECM patterns regulate the cell division axis.[91] [Reprinted by permission from Macmillan Publishers Ltd: Nature, 447:493–496, copyright 2007].
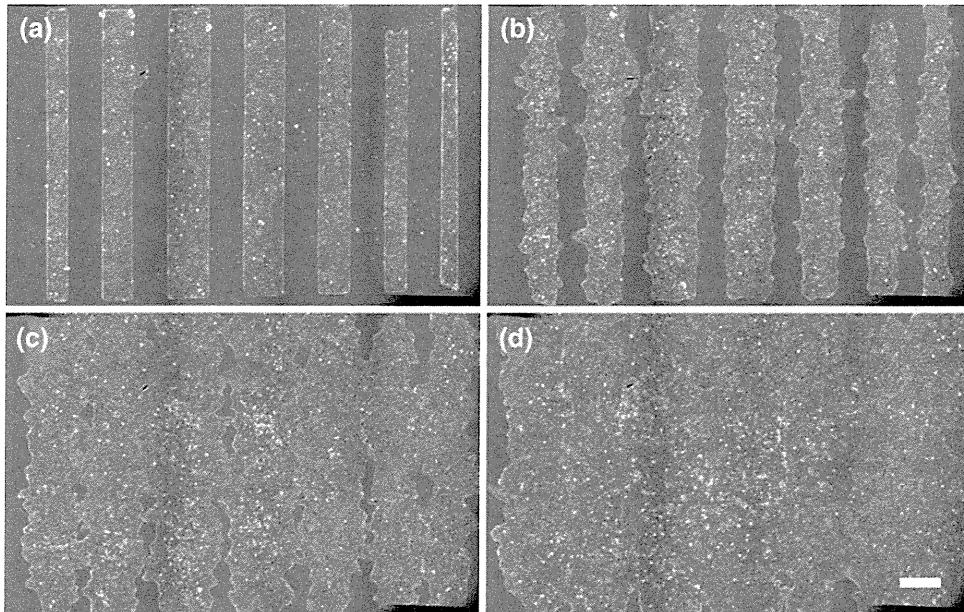
FIGURE 3. A microstencil based method to produce a multiple models of wounds for collective cell migration study.[80] [Copyright 2007 National Academy of Sciences, USA].

Collective cell migration is relevant to several important biological processes such as wound healing and cancer metastasis. Recently, a micro-fabricated soft elastic "microstencil" was used to study wound healing by first placing it on a cell culture surface.[80] Once cells had grown to confluence within the stencil, the stencil was then lifted off which resulted in multiple injury-free wounds for cell migration observation (Fig. 3). Here, cell migration behaviors were characterized as both collective and individualistic. While many cells moved in a collective and coordinated way, there were some very active "leader cells" fingering the borders and acting in a very fibroblast-like and non-epithelial manner.

Micropillar Assays

The micropillars are typically made of PDMS and the corresponding assays consist of arrays of pillars whose stiffness is controlled by their diameter, height, and curing conditions. Also, the tips of these micropillars are coated with ECM proteins to allow for effective attachment and migration of cells on top of these pillars.

Micropillared substrate is often used to characterize cellular traction forces by observing the extent to which the cells deflect the micropillars. They have been used to measure traction forces exerted by epithelial cells sheets[24] as well as single migrating cells. Other examples include the use of micropillar substrate to probe the chemo-mechanical effects of anti-cancer drugs such as emodin on cancer cells.[102]

Apart from measuring cellular traction forces, micropillar substrates have also been used for
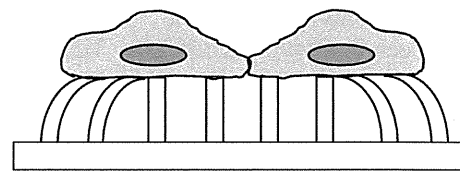

FIGURE 4. Two cells on fibronectin stamped micropillar substrate form an intercellular adhesion. The force of intercellular adhesion is equal and opposite to the sum of the forces exerted by each single cell on the micropillars.

characterizing the intercellular adhesion forces between cells. Here, micropillars were first microcontact printed with a "bowtie" pattern of fibronectin.[56] Cells were subsequently allowed to adhere and spread on these patterns and the cell substrate traction forces were determined from the deflection of the micropillars (Fig. 4). Using this technique it was shown that mechanical tugging force regulated the size of intercellular adhesion.

Modeling and Simulations

Actin Dynamics in Migrating Cell: Molecular-Scale Modeling Approaches

Cell migration is a crucial process for many physiological and pathological events, such as embryogenesis and cancer metastasis. During cell migration, a lamellipodium is formed, which is a flat and broad membrane extension filled with a dense and highly branched actin network.[87,96] Protrusion of the lamellipodial leading edge, referred to as membrane protrusion,

is one of the essential cellular activities for continuous cell migration because it brings the front margin of the migrating cell forward.[51] During membrane protrusion, branched actin filaments are polarized with their barbed ends in the migrating direction and polymerized beneath the membrane. The chemical energy gain from the polymerization is consumed by mechanical work of the membrane protrusion.[8,79]

To explain the mechanochemical aspect of force generation that drives membrane protrusion, a mathematical model has been constructed: the Brownian ratchet (BR).[67,77] According to the BR, the membrane in front of the actin filament is thermally fluctuated in its position. The membrane fluctuations create a sufficient gap for monomers to intercalate and to polymerize at the barbed end. Thus, the polymerized actin filaments beneath the membrane rectify the Brownian motion of the membrane so as to produce a unidirectional force. Subsequent modeling extends the BR to flexible actin filaments: the elastic BR. If the actin filament is long, its own thermal undulations can also create a gap between its barbed end and the membrane.[68] By applying the BR models, the protrusion velocity of not only lamellipodia[66,67] but also filopodia[3,69] has been analyzed successfully. The fundamental understanding of these molecular machineries has attracted new interests regarding their relationships with cellular behaviors over several spatial and temporal scales.

Non-muscle myosin II and actin constitute the major force-generating machinery of actomyosin networks, where actomyosin contractility is fundamental to cellular reshaping and movement.[97] Therefore, these mechanical behaviors of actomyosin networks are recognized as being fundamental to biological functions,[54] but the mechanochemical basis of the emergence of these functions is still unclear.

At the individual actin filament level, several mathematical models of actin networks, such as semi-flexible polymers without cross-links[90] and with cross-links[37,45] have been proposed. These models have successfully simulated the dynamics of actin networks and clarified its relationship with rheological properties, whereas processive myosin movements which is the origin of the contractility of actomyosin networks, has not been considered. On the other hand, at the cellular-scale, the cable network model (CNM) has been suggested for studying contractile actin networks, which has demonstrated that the mechanics of a contractile filamentous network with a spatial distribution of adhesions is important in determining cellular shape.[75] Because the CNM relies on a lattice discretization of the mean field of the actin cytoskeleton, it illustrates the computational efficiency for cellular-scale simulations. However, the cables described in the CNM are not meant to represent individual actin filaments. Therefore, analyzing the dynamic rearrangement of actomyosin networks is beyond the scope of the CNM. Gathering and extending these mathematical models at the individual filament level, it gives challenging opportunities for better understanding of force generation and dynamic rearrangement in actomyosin networks.

Actin-Based Cell Motility: Cellular-Scale Modeling Approaches

Recently, several experiments have been performed to relate actin dynamics in migrating cell with cellular-scale activities such as the shapes of migrating cells.[43,49,104] To enhance the knowledge of these multiscale relationships, theoretical and computational studies at the whole-cell level are needed.

Several studies to construct whole-cell models and simulate cell migration involved with various cell shapes have been reported. Rubinstein *et al.* have proposed the 2D model of the fish keratocyte.[81] This model incorporates lamellipodial protrusion, cell adhesion, contraction and actin transport. The simulations using the model reproduce observed cell shapes, forces, and movements qualitatively, and give an explanation about some experimental results of perturbations on the actin machinery. For example, it has been observed experimentally that photoreleasing a caged thymosin at one side of a keratocytes lamellipodium induces a pivotal motion of the keratocytes around the perturbed side. The model has successfully explained this cellular response to the perturbation from the view point of G-actin concentration. Maree *et al.* have suggested a 2D whole-cell model of the fish keratocyte based on the cellular potts model that stochastically determines the leading edge protrusion where force–velocity relation in the protrusion is fitted to the thermal ratchet force–velocity curve in the model.[62] In addition, their model takes into account the effects of some chemical signal transductions such as Cdc42, Rac, and Rho. The model gives an insight into how the keratocyte can maintain its shape and polarity and how it can alter direction in response to changes in its environment in terms of interactions of Cdc42, Rac and Rho.

However, these models are phenomenological and not derived on the basis of the underlying molecular mechanism that has been considered by the BR. Although the cellular-scale simulations using the BR with a membrane load has been analyzed,[31,66] it is unable to be used for studies in which resultant shapes of the cells are unknown. This is because the BR requires *a priori* constant load that depends on the cell shape.

Recently, Inoue and Adachi have suggested a 2D keratocyte model based on the coarse-grained BR that
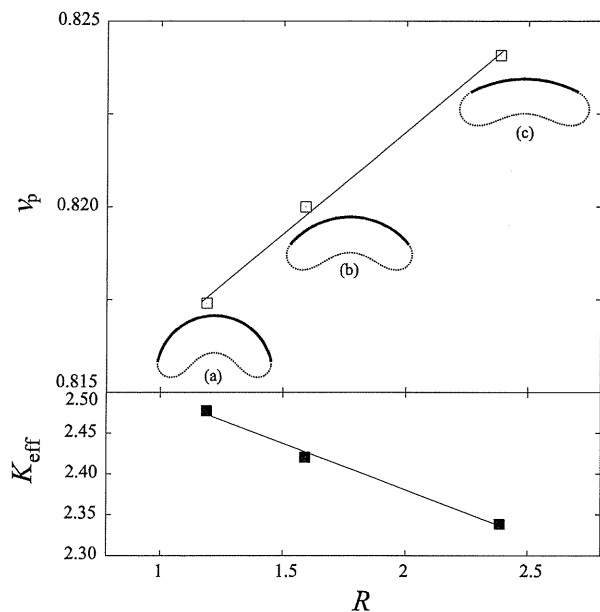
FIGURE 5. Protrusion velocity, v_p, and effective elastic constant of the leading edge, K_{eff}, measured in 10^6 $k_BT/\mu m^2$ as a function of the radius of the curvature of the leading edge, R (μm). The radius is obtained by a least square fitting of the equation of a circle to a set of positional vectors of nodes allocated to the leading edge. Open and solid squares indicate the values of v_p and K_{eff}, respectively. All lines are only for the sake of reference. Simulated shapes of the leading edge are indicated by the solid line, wherein a critical stall velocity is 0.80 (a), 0.81 (b), and 0.82 (c).

is derived using non-equilibrium thermodynamics theory on the basis of the underlying molecular mechanism.[39] Because they assume that the cell is either stationary or steady migrating, the cell adhesion and contraction can be simply expressed in terms of an energy constraint at the cellular level. This model estimates the protrusion velocity, v_p, consistently with an effective elastic constant, K_{eff}, which represents the state of the energy of the membrane, and reproduces the experimentally-observed keratocyte shapes by the simulation (Fig. 5). The trend of dependences of the protrusion velocity on the curvature of the leading edge, the temperature, and the substrate stiffness has also agreed with the other experimental results.

While these mathematical modeling of cell migrations have achieved significant success, they are still 2D models. Thus, further efforts should now focus on investigating 3D environments.

MOLECULAR BIOMECHANICS AND MECHANOCHEMISTRY

Molecular biomechanics focuses on how a single molecule behaves mechanically and/or how two counterpart molecules interact with each other, while mechanochemistry refers to how mechanical stimuli

(enforced contact, restrained fluctuation, shear flow, etc) regulate the conformational changes of biomolecules and affect their biochemical reactions and biological functions.

Experimental Techniques

Micropipette Aspiration

Micropipette aspiration technique (MAT) was first used in quantifying the mechanical and viscoelastic properties of an isolated cell in the mid-1950s when a suction pressure was applied on the cell *via* a pipette. In the past two decades, MAT has been widely employed to understand the binding kinetics and rupture force of surface-bound receptor–ligand interactions using two experimental protocols: the adhesion frequency assay (*left panel*) and the biomembrane force probe (BFP) assay (*right panel*) (Fig. 6a). Data analysis is conducted on the measured data to predict the kinetic rate/binding affinity and rupture force/bond lifetime. In the adhesion frequency assay, the adhesion frequency, defined as the fraction of adhesive events over the total number of tests conducted and measured over the systematically-varied contact duration and site densities of receptors and ligands, are predicted using a probabilistic model of small system kinetics[15] to collect the forward and reverse rates and binding affinity.[35,101] In the biomembrane force probe assay, the rupture force, defined as the product of membrane deflection and membrane stiffness, is measured on the systematically varied loading rate. Dynamic force spectroscopy (DFS) theorem that defines the correlation of rupture force to loading rate[25] is then used to predict the parameters of energy landscape upon Bell model.[4] Bond lifetime, defined as the time interval during which the bond remains bound, is measured on the systematically-varied applied force. A first-order dissociation kinetics model is then used to predict the reverse rate or bond lifetime.

MAT and BFP assays have been widely applied to test various adhesive molecular pairs, such as FcγR-IgG,[15] selectin–ligand,[35,101] integrin–ligand,[107] and TCR-MHCII binding.[36] While at least one type of molecule of interest needs to be purified from the cell membrane and re-captured onto a RBC or bead as a force transducer in these conventional assays, a gas-driven MAT newly-developed is able to determine directly the binding kinetics of interacting molecules constitutively expressed on nucleated cells (*left panel* in Fig. 6a).

Optical Tweezers Manipulation

Optical tweezers (OT) assay was first applied by trapping the biological particles in the late 1980s.[2] An
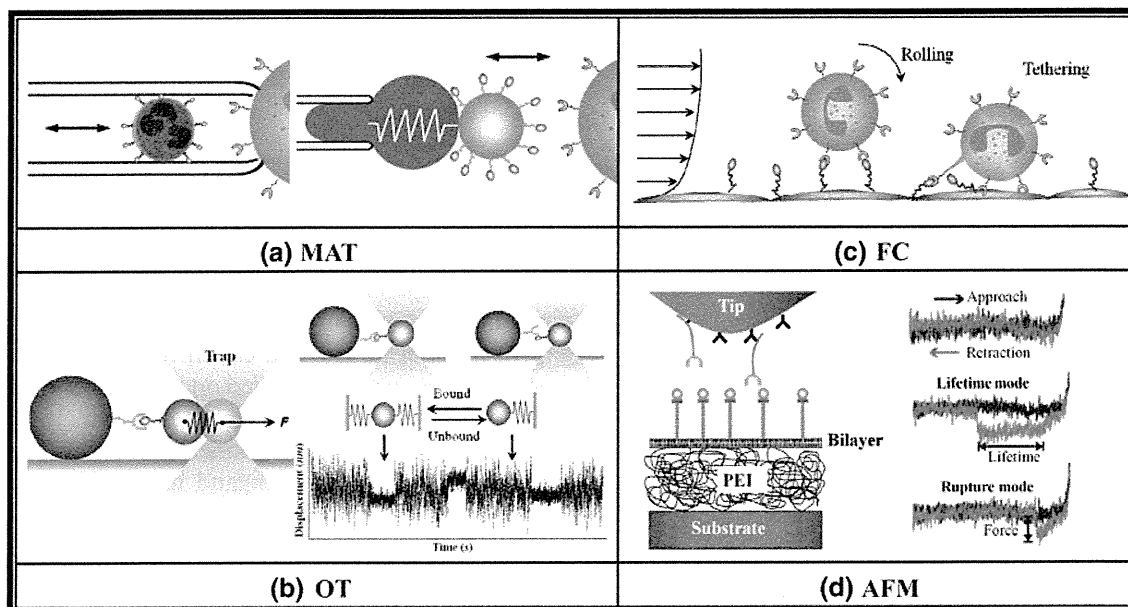
FIGURE 6. Schematics of MAT (a), OT (b), FC (c), and AFM (d) assays. (a) A gas driven MAT assay (left) and a BFP assay (right). (b) An OT assay for monitoring bond rupture (left) and association kinetics (right). (c) A FC assay for neutrophils rolling (left) and tethering (right). (d) An AFM assay for system functioning (left) and working protocols (right).

adhesive event is identified when the bead/cell is bounced back to the trap center during withdrawal (*left panel* in Fig. 6b). The advantage of OT assay lies in its features of non-contact, low perturbation, and high spatial and temporal resolutions, which enables one to conduct the delicate, near-equilibrium tests for unbinding and association kinetics of molecular pair of interest. The protocol for unbinding kinetics is the same as that done in MAT assay. The other for association kinetics has been recently developed based upon the thermal fluctuation rationale (*right panel* in Fig. 6b),[88] in which the time course of bead displacement is monitored for the occurrence of sequential binding and unbinding events, as is also observed in BFP[11] assay. To date, OT assay has been widely applied in many molecular systems to understand the molecular biomechanics and biophysics at a highly-sensitive resolution.

Parallel Flow Chamber

Parallel flow chamber (FC) technique, similar to that mentioned earlier for studying cell mechanics, has also been applied to quantify the molecular mechanics of cell rolling.[41] A laminar flow is usually applied to drive a receptor-expressing cell/bead flowing over the ligand-immobilized substrate or surface. Time course of the binding of cell/bead is visualized when it encounters the substrate and various adhesion patterns are identified mainly as rolling (*left panel*) and (transient) tethering (*right panel*) (Fig. 6c) of the flowing

cell/bead. Collected cell accumulation, detachment, tethering and rolling, and transient rolling, are then used to determine the kinetics of interacting molecules under systematically-varied shear stress and site density of interacting molecules. A first-order dissociation kinetics model that defines the irreversible unbinding is used to predict the bond lifetime at a given shear stress, together with Bell's model for the force dependence of bond lifetime.

FC serves as an *in vitro* assay to mimic the physiological flow in many biological processes such as inflammatory cascade, tumor metastasis, and thrombus formation. It has been widely used to understand the cell rolling over and tethering on the substrate mediated by receptor–ligand interactions under blood flow.

Atomic Force Microscopy

Atomic force microscopy (AFM) was first developed in the mid 1980s based upon the scanning tunnel microscope.[7] An adhesive event is identified when the cantilever is deflected during withdrawal (*left panel* in Fig. 6d), and the measured data is employed to predict the rupture force/bond lifetime. Two modes are applied to quantify the mechanochemistry of receptor–ligand bond under applied force: the rupture force mode works at a given loading rate while the bond lifetime mode operates at a given applied force (*right panel* in Fig. 6d). Mechano-chemical coupling models that define the dependence of reverse rate on applied

force,[4,19] together with DFS theorem,[25] are then used to predict the parameters of kinetic rates and energy landscape.

AFM assay has now been widely applied to understand the forced dissociation at the single molecule level. By combining with micro-fabricated technologies, it is also possible to build up an AFM array to probe the multiple events or species simultaneously.

Simulations and Modeling

Molecular Dynamic Simulation of Molecular Biomechanics

By incorporating both conformational changes and atomic details of biomolecules in a 3D environment with different temperatures, pressures, and/or mechanical constraints, molecular dynamics simulation (MDS) provides functional implication and yields information that is not possible through any other means.[1] Today, MDS is routinely applied in investigating the respective mechano-chemical coupling and mechanical properties of biomolecules at the single molecular level.[1] Variable simulation protocols and analysis methods such as free,[59] steered,[78] and flow molecular dynamics,[59] have been developed to manifest the interesting properties of biomolecules.

Classical or free MDS has been widely used to probe conformational stability, flexibility, and folding/unfolding pathway of proteins. For example, the instability of GPIbα β-hairpin without vWF is demonstrated by a free MDS as a spontaneous transition to a structureless loop.[59] But for vWF-A1/GPIbα complex, MDS exhibits its conformational flexibility and the stabilizing electrostatic interactions between these two proteins.[40] The unfolding of the central β-sheet of vWF-A2 is proposed to start from its edges and then propagate into its center.[13] The allostery of P-selectin lectin (Lec) domain followed by an epithelial growth factor (EGF)-like domain is recently visualized using free MDS.[61] These simulations shed light on the question that what aspects, such as topology, hydrogen-bonding patterns, and core interactions, determine the mechanical properties of a protein.[26]

Compared with free MDS, a steered molecular dynamics (SMD) simulation is more popular in investigating mechano-chemical coupling and mechanical properties of biomolecules due to the inherent similarity to AFM, OT, and BFP assays as well as DFS experiments. In SMD, external forces are applied to molecules to probe their mechanical properties, as well as to accelerate processes that are otherwise too slow to model.[78] As an *in silico* complement of single-molecule techniques, SMD simulations have been extensively used in many studies.

Lü and Long have applied SMD to stretch a single P-selectin construct and suggested that the burst of intramolecular hydrogen bonds is the main cause of the structural collapses.[60] From simulation of unfolding of vWF A domains by tensile force, Chen *et al.* have observed two different unfolding pathways of β-strands, the sliding and unzipping pathways being encountered by higher and lower energy barriers, respectively.[12] Liu *et al.* have estimated the elastic modulus of antimicrobial peptide HP(2-20) and its four analogues through SMD and further proposed a rigidity-enhanced antimicrobial activation of the peptides.[55] SMD simulations on unbinding of receptor from its ligand, such as P-selectin glycoprotein ligand 1 (PSGL-1) from P-selectin and glycoprotein Ibα (GPIbα) from vWF-A1, have provided insights into the molecular mechanism underlying catch-bond.[32,40,58,103]

Flow MDS was inspired from FC assay and first carried out by Lou and Zhu[59] and further improved by Chen *et al.*[14] Upon flow MDS, the authors have observed the significant conformational change on the β-switch of GPIbα extracellular domain, and suggested a structural explanation of flow-enhanced affinity of GPIbα and vWF.[59] Zou *et al.* have compared a coarse-lattice model and a freely jointed chain model so as to illustrate how the folding rate and conformational transition of β-hairpin depend on the entropic and enthalpic energies, the latter controlled by flow show.[109] Wang and Sandberg[98] have observed the unfolding of ubiquitin through flow MDS, in which flow is generated by pulling two frozen water surfaces along a given direction. These results have exhibited potential ability of flow MDS in modeling biological process under flow at the single molecular level.

The timescale of MD simulation generally yields several nanoseconds, but the experimental time window (or dynamical range) is about 10 ms, 1 ms, or 10 μs for optical tweezers, BFP, or AFM techniques, respectively. This timescale gap of 3-6 magnitude orders between MDS and single biomolecular experiments has certainly limited the application of MD. Recently, several studies with individual trajectories longer than one microsecond have been reported.[46] The gap is becoming narrower with the improvements in molecular dynamics algorithms, software, and computer hardware.

Mathematical Modeling on Receptor–Ligand Binding in Cell Adhesion

As a key step in many physiological processes, cell adhesion under flow is a mechanochemical coupling process, including initial tethering, rolling, and firm adhesion, and is mediated by receptor–ligand interaction.[106] Attention has been paid to theoretical

modeling on force-dependent receptor–ligand binding in cell adhesion, in order to better understand the events of cell adhesion and extract reaction kinetic information of adhesive molecules from measured data.

Bell model, the best-known theoretical model derived from thermodynamic analysis on specific adhesive events between the cells, demonstrates slip-bond mechanism of receptor–ligand interaction under applied forces,[4,5] but fails to describe catch-bond behavior which governs flow-enhanced cell adhesion. Two-pathway model and deformation model are developed to depict the transition from catch-bond to slip-bond in receptor–ligand interaction under forces.[32] Force-dependent association models have provided a way to estimate reverse rate of receptor unbinding from its ligand in AFM, OT, and BFP assays as well as DFS measurements. To date, the force dependence of reverse rate of receptor–ligand interaction has been intensively studied by different methods, including lifetime and rupture force measurements of single bonds or tether and rupture force measurements of single cell.[11]

Cell adhesion mediated by receptor–ligand interaction refers to a 2D kinetic process at the cell contact area. Currently, it is still a challenge to relate molecular binding kinetics measured in 3D conditions to that in 2D or membrane-bound cases. Both probabilistic and deterministic models have been developed in the past decades. For example, Chesla et al. have developed a probabilistic model of molecular kinetics for a small system with a few bonds (most likely one) forming during a contact with short duration and low densities of both receptors and ligands on the apposing surfaces.[15] By contrast, Wu et al.[100] have used a deterministic description of force-free, coupled reaction–diffusion model to determine 2D kinetics of receptor–ligand interaction in a contact-area FRAP (fluorescence recovery after photobleaching) assay where sufficient bonds in contact area are required in stable cell adhesion. The association rate so measured from any one of above two assays is a lumped parameter with contact area, which is usually unknown in MAT,[15] but can be roughly estimated in FRAP measurements.[100]

Modeling for cell adhesion mediated by receptor–ligand interactions under flow has long been attractive to investigators. In the adhesive dynamics model introduced by Hammer and Apte,[33] the balance of forces and torques on a cell flowing near a surface due to hydrodynamic shear and ligand–receptor bonds has been considered for cell adhesion on vessel wall and the cell movements from free flowing, tethering, rolling motion to firm adhesion are well modeled.[6,9,10,47,48] Moreover, Long et al.[57] have developed a probabilistic model, instead of Monte Carlo simulation, to simulate the shear-induced formation and breakage of doublets

cross-linked by receptor–ligand bonds for cell aggregation inside blood vessel. Cellular properties including microvilli tethering and cytoskeletal deformation are important in mediating cell rolling.[105] To examine the dynamic contact forces on leukocyte microvilli, Zhao et al. have presented a theoretical model and predicted that contact force increases nonlinearly with shear and that only the longest microvilli contacts the substrate at high shear stress >0.2 dyn/cm^2.[108] Yu and Shao have further developed a model to understand the effect of cell membrane tether extraction on neutrophil rolling stabilization and indicated that simultaneous tether extraction from the neutrophil and endothelial cell increases bond lifetime, which has made more transient tethers to be stable and then let rolling neutrophils to be more shear-resistant.[105] Pawar et al. have modeled cell body and microvillus deformation and predicted that both catch-slip-bond behavior and lesser cell deformation are responsible for threshold phenomenon observed on selectin-mediated leukocyte rolling over ligand-immobilized substrate under shear flow.[76]

CONCLUDING REMARKS

In this mini-review, we briefly reported the recent advances in the experimental and modeling aspects of micro- and nano-biomechanics research. These developments are helpful in enabling us to further understand the mechanisms involved in cell mechanics and mechanobiology as well as molecule biomechanics and mechanochemistry.

It is hoped that in the near future and with further progress made in this area, we will be able to better integrate the information obtained at the cell and molecular levels and provide a clearer insight into the mechanical transduction and signaling from cell to biomolecule and vice versa. Such findings will certainly be helpful in further elucidating the basic functions of biological systems at the cellular and molecular levels.

ACKNOWLEDGMENT

REFERENCES

[1]Adcock, S. A., and J. A. McCammon. Molecular dynamics: survey of methods for simulating the activity of proteins. Chem. Rev. 106:1589–1615, 2006.

[2]Ashkin, A., J. M. Dziedzic, and T. Yamane. Optical trapping and manipulation of single cells using infrared-laser beams. *Nature* 330:769–771, 1987.

[3]Atilgan, E., D. Wirtz, and S. X. Sun. Mechanics and dynamics of actin-driven thin membrane protrusions. *Biophys. J.* 90:65–76, 2006.

[4]Bell, G. I. Models for specific adhesion of cells to cells. *Science* 200:618–627, 1978.

[5]Bell, G. I., M. Dembo, and P. Bongrand. Cell adhesion. Competition between nonspecific repulsion and specific bonding. *Biophys. J.* 45:1051–1064, 1984.

[6]Bhatia, S. K., M. R. King, and D. A. Hammer. The state diagram for cell adhesion mediated by two receptors. *Biophys. J.* 84:2671–2690, 2003.

[7]Binnig, G., C. F. Quate, and C. Gerber. Atomic force microscope. *Phys. Rev. Lett.* 56:930–933, 1986.

[8]Borisy, G. G., and T. M. Svitkina. Actin machinery: pushing the envelope. *Curr. Opin. Cell Biol.* 12:104–112, 2000.

[9]Caputo, K. E., and D. A. Hammer. Adhesive dynamics simulation of G-protein-mediated chemokine-activated neutrophil adhesion. *Biophys. J.* 96:2989–3004, 2009.

[10]Chang, K. C., D. F. J. Tees, and D. A. Hammer. The state diagram for cell adhesion under flow: leukocyte rolling and firm adhesion. *Proc. Natl Acad. Sci. USA* 97:11262–11267, 2000.

[11]Chen, W., E. A. Evans, R. P. McEver, and C. Zhu. Monitoring receptor–ligand interactions between surfaces by thermal fluctuations. *Biophys. J.* 94:694–701, 2008.

[12]Chen, W., J. Z. Lou, and C. Zhu. Molecular dynamics simulated unfolding of von Willebrand factor A domains by force. *Cell. Mol. Bioeng.* 2:75–86, 2009.

[13]Chen, W., J. Z. Lou, and C. Zhu. Simulated thermal unfolding of the von Willebrand factor A domains. *Cell. Mol. Bioeng.* 3:117–127, 2010.

[14]Chen, Z., J. Z. Lou, C. Zhu, and K. Schulten. Flow-induced structural transition in the beta-switch region of glycoprotein Ib. *Biophys. J.* 95:1303–1313, 2008.

[15]Chesla, S. E., P. Selvaraj, and C. Zhu. Measuring two-dimensional receptor–ligand binding kinetics by micropipette. *Biophys. J.* 75:1553–1572, 1998.

[16]Chiu, J. J., C. N. Chen, P. L. Lee, C. T. Yang, H. S. Chuang, et al. Analysis of the effect of disturbed flow on monocytic adhesion to endothelial cells. *J. Biomech.* 36:1883–1895, 2003.

[17]Davies, P. F., A. Remuzzi, E. J. Gordon, C. F. Dewey, Jr., and M. A. Gimbrone, Jr. Turbulent fluid shear stress induces vascular endothelial cell turnover in vitro. *Proc. Natl Acad. Sci. USA* 83:2114–2117, 1986.

[18]del Rio, A., R. Perez-Jimenez, R. C. Liu, P. Roca-Cusachs, J. M. Fernandez, et al. Stretching single talin rod molecules activates vinculin binding. *Science* 323:638–641, 2009.

[19]Dembo, M., D. C. Torney, K. Saxman, and D. Hammer. The reaction-limited kinetics of membrane-to-surface adhesion and detachment. *Proc. R. Soc. Lond. B Biol. Sci.* 234:55–83, 1988.

[20]Deng, L. H., N. J. Fairbank, B. Fabry, P. G. Smith, and G. N. Maksym. Localized mechanical stress induces time-dependent actin cytoskeletal remodeling and stiffening in cultured airway smooth muscle cells. *Am. J. Physiol. Cell Physiol.* 287:C440–C448, 2004.

[21]DePaola, N., P. F. Davies, W. F. Pritchard, L. Florez, N. Harbeck, et al. Spatial and temporal regulation of gap junction connexin43 in vascular endothelial cells exposed to controlled disturbed flows in vitro. *Proc. Natl Acad. Sci. USA* 96:3154–3159, 1999.

[22]Dewey, C. F., S. R. Bussolari, M. A. Gimbrone, and P. F. Davies. The Dynamic response of vascular endothelial-cells to fluid shear-stress. *J. Biomech. Eng.* 103:177–185, 1981.

[23]Doyle, A. D., F. W. Wang, K. Matsumoto, and K. M. Yamada. One-dimensional topography underlies three-dimensional fibrillar cell migration. *J. Cell Biol.* 184:481–490, 2009.

[24]du Roure, O., A. Saez, A. Buguin, R. H. Austin, P. Chavrier, et al. Force mapping in epithelial cell migration. *Proc. Natl Acad. Sci. USA* 102:2390–2395, 2005.

[25]Evans, E., K. Ritchie, and R. Merkel. Sensitive force technique to probe molecular adhesion and structural linkages at biological interfaces. *Biophys. J.* 68:2580–2587, 1995.

[26]Forman, J. R., and J. Clarke. Mechanical unfolding of proteins: insights into biology, structure and folding. *Curr. Opin. Struct. Biol.* 17:58–66, 2007.

[27]Frangos, J. A., L. V. McIntire, and S. G. Eskin. Shear stress induced stimulation of mammalian cell metabolism. *Biotechnol. Bioeng.* 32:1053–1060, 1988.

[28]Frye, S. R., A. Yee, S. G. Eskin, R. Guerra, X. Y. Cong, et al. CDNA microarray analysis of endothelial cells subjected to cyclic mechanical strain: importance of motion control. *Physiol. Genomics* 21:124–130, 2005.

[29]Galbraith, C. G., R. Skalak, and S. Chien. Shear stress induces spatial reorganization of the endothelial cell cytoskeleton. *Cell Motil. Cytoskeleton* 40:317–330, 1998.

[30]Galbraith, C. G., K. M. Yamada, and M. P. Sheetz. The relationship between force and focal complex development. *J. Cell Biol.* 159:695–705, 2002.

[31]Grimm, H. P., A. B. Verkhovsky, A. Mogilner, and J. J. Meister. Analysis of actin dynamics at the leading edge of crawling cells: implications for the shape of keratocyte lamellipodia. *Eur. Biophys. J.* 32:563–577, 2003.

[32]Gunnerson, K. N., Y. V. Pereverzev, and O. V. Prezhdo. Atomistic simulation combined with analytic theory to study the response of the P-selectin/PSGL-1 complex to an external force. *J. Phys. Chem. B* 113:2090–2100, 2009.

[33]Hammer, D. A., and S. M. Apte. Simulation of cell rolling and adhesion on surfaces in shear-flow. General results and analysis of selectin-mediated neutrophil adhesion. *Biophys. J.* 63:35–57, 1992.

[34]Hayakawa, K., H. Tatsumi, and M. Sokabe. Actin stress fibers transmit and focus force to activate mechanosensitive channels. *J. Cell Sci.* 121:496–503, 2008.

[35]Huang, J., J. Chen, S. E. Chesla, T. Yago, P. Mehta, et al. Quantifying the effects of molecular orientation and length on two-dimensional receptor–ligand binding kinetics. *J. Biol. Chem.* 279:44915–44923, 2004.

[36]Huang, J., V. I. Zarnitsyna, B. Y. Liu, L. J. Edwards, N. Jiang, et al. The kinetics of two-dimensional TCR and pMHC interactions determine T-cell responsiveness. *Nature* 464:932–936, 2010.

[37]Huisman, E. M., T. van Dillen, P. R. Onck, and E. Van der Giessen. Three-dimensional cross-linked F-actin networks: relation between network architecture and mechanical behavior. *Phys. Rev. Lett.* 99:208103, 2007.

[38]Icard-Arcizet, D., O. Cardoso, A. Richert, and S. Henon. Cell stiffening in response to external stress is correlated to actin recruitment. *Biophys. J.* 94:2906–2913, 2008.

[39]Inoue, Y., and T. Adachi. Coarse-grained Brownian ratchet model of membrane protrusion on cellular scale. *Biomech. Model. Mechanobiol.*, 2010. doi:10.1007/s10237-010-0250-6.

[40]Interlandi, G., and W. Thomas. The catch bond mechanism between von Willebrand Factor and platelet surface receptors investigated by molecular dynamics simulations. *Proteins* 78:2506–2522, 2010.

[41]Kaplanski, G., C. Farnarier, O. Tissot, A. Pierres, A. M. Benoliel, et al. Granulocyte endothelium initial adhesion—analysis of transient binding events mediated by E-selectin in a laminar shear-flow. *Biophys. J.* 64:1922–1933, 1993.

[42]Kataoka, N., S. Ujita, and M. Sato. Effect of flow direction on the morphological responses of cultured bovine aortic endothelial cells. *Med. Biol. Eng. Comput.* 36:122–128, 1998.

[43]Keren, K., Z. Pincus, G. M. Allen, E. L. Barnhart, G. Marriott, et al. Mechanism of shape determination in motile cells. *Nature* 453:475–480, 2008.

[44]Kilian, K. A., B. Bugarija, B. T. Lahn, and M. Mrksich. Geometric cues for directing the differentiation of mesenchymal stem cells. *Proc. Natl Acad. Sci. USA* 107:4872–4877, 2010.

[45]Kim, T., W. Hwang, H. Lee, and R. D. Kamm. Computational analysis of viscoelastic properties of crosslinked actin networks. *PLoS Comput. Biol.* 5:e1000439, 2009.

[46]Klepeis, J. L., et al. Long-timescale molecular dynamics simulations of protein structure and function. *Curr. Opin. Struct. Biol.* 19(2):120–127, 2009.

[47]Krasik, E. F., K. E. Caputo, and D. A. Hammer. Adhesive dynamics simulation of neutrophil arrest with stochastic activation. *Biophys. J.* 95:1716–1728, 2008.

[48]Krasik, E. F., K. L. Yee, and D. A. Hammer. Adhesive dynamics simulation of neutrophil arrest with deterministic activation. *Biophys. J.* 91:1145–1155, 2006.

[49]Lacayo, C. I., Z. Pincus, M. M. VanDuijn, C. A. Wilson, D. A. Fletcher, et al. Emergence of large-scale cell morphology and movement from local actin filament growth dynamics. *PLoS Biol.* 5:2035–2052, 2007.

[50]LaMack, J. A., and M. H. Friedman. Individual and combined effects of shear stress magnitude and spatial gradient on endothelial cell gene expression. *Am. J. Physiol. Heart Circ. Physiol.* 293:H2853–H2859, 2007.

[51]Lauffenburger, D. A., and A. F. Horwitz. Cell migration: a physically integrated molecular process. *Cell* 84:359–369, 1996.

[52]Levesque, M. J., and R. M. Nerem. The elongation and orientation of cultured endothelial cells in response to shear stress. *J. Biomech. Eng.* 107:341–347, 1985.

[53]Levesque, M. J., R. M. Nerem, and E. A. Sprague. Vascular endothelial-cell proliferation in culture and the influence of flow. *Biomaterials* 11:702–707, 1990.

[54]Li, S., J. L. Guan, and S. Chien. Biochemistry and biomechanics of cell motility. *Annu. Rev. Biomed. Eng.* 7:105–150, 2005.

[55]Liu, L., Y. Fang, Q. Huang, and J. Wu. A rigidity-enhanced antimicrobial activity: a case for linear cationic alpha-helical peptide HP(2–20) and its four analogues. *PLoS One* 6(1):e16441, 2011.

[56]Liu, Z., J. L. Tan, D. M. Cohen, M. T. Yang, N. J. Sniadecki, et al. Mechanical tugging force regulates the size of cell–cell junctions. *Proc. Natl Acad. Sci. USA* 107:9944–9949, 2010.

[57]Long, M., H. L. Goldsmith, D. F. J. Tees, and C. Zhu. Probabilistic modeling of shear-induced formation and breakage of doublets cross-linked by receptor–ligand bonds. *Biophys. J.* 76:1112–1128, 1999.

[58]Lou, J. Z., and C. Zhu. A structure-based sliding–rebinding mechanism for catch bonds. *Biophys. J.* 92:1471–1485, 2007.

[59]Lou, J. Z., and C. Zhu. Flow induces loop-to-beta-hairpin transition on the beta-switch of platelet glycoprotein Ib alpha. *Proc. Natl Acad. Sci. USA* 105:13847–13852, 2008.

[60]Lü, S. Q., and M. Long. Forced extension of P-selectin construct using steered molecular dynamics. *Chin. Sci. Bull.* 49:10–17, 2004.

[61]Lü, S. Q., Y. Zhang, and M. Long. Visualization of allostery in P-selectin lectin domain using MD simulations. *PLoS One* 5(12):e15417, 2010.

[62]Maree, A. F. M., A. Jilkine, A. Dawes, V. A. Grieneisen, and L. Edelstein-Keshet. Polarization and movement of keratocytes: a multiscale modelling approach. *Bull. Math. Biol.* 68:1169–1211, 2006.

[63]Matthews, B. D., D. R. Overby, R. Mannix, and D. E. Ingber. Cellular adaptation to mechanical stress: role of integrins, Rho, cytoskeletal tension and mechanosensitive ion channels. *J. Cell Sci.* 119:508–518, 2006.

[64]McBeath, R., D. M. Pirone, C. M. Nelson, K. Bhadriraju, and C. S. Chen. Cell shape, cytoskeletal tension, and RhoA regulate stem cell lineage commitment. *Dev. Cell* 6:483–495, 2004.

[65]Metaxa, E., H. Meng, S. R. Kaluvala, M. P. Szymanski, R. A. Paluch, et al. Nitric oxide-dependent stimulation of endothelial cell proliferation by sustained high flow. *Am. J. Physiol. Heart Circ. Physiol.* 295:H736–H742, 2008.

[66]Mogilner, A., and L. Edelstein-Keshet. Regulation of actin dynamics in rapidly moving cells: a quantitative analysis. *Biophys. J.* 83:1237–1258, 2002.

[67]Mogilner, A., and G. Oster. Cell motility driven by actin polymerization. *Biophys. J.* 71:3030–3045, 1996.

[68]Mogilner, A., and G. Oster. Force generation by actin polymerization II: the elastic ratchet and tethered filaments. *Biophys. J.* 84:1591–1605, 2003.

[69]Mogilner, A., and B. Rubinstein. The physics of filopodial protrusion. *Biophys. J.* 89:782–795, 2005.

[70]Morigi, M., C. Zoja, M. Figliuzzi, M. Foppolo, G. Micheletti, et al. Fluid shear-stress modulates surface expression of adhesion molecules by endothelial-cells. *Blood* 85:1696–1703, 1995.

[71]Nagel, T., N. Resnick, C. F. Dewey, and M. A. Gimbrone. Vascular endothelial cells respond to spatial gradients in fluid shear stress by enhanced activation of transcription factors. *Thromb. Vasc. Biol.* 19:1825–1834, 1999.

[72]Nakaya, M., M. Kitano, M. Masuda, and S. Nagata. Spationtemporal activation of Rac1 for engulfment of apoptotic cells. *Proc. Natl Acad. Sci. USA* 195:9198–9203, 2008.

[73]Nishio, K., Y. Ueki, N. Sakamoto, and M. Sato. Effect of initial orientation of vascular endothelial cells on activation of RhoGTPases induced by fluid shear stress. *Cell. Mol. Bioeng.* 2:160–168, 2011.

[74]Nomura, H., C. Ishikawa, T. Komatsuda, J. Ando, and A. Kamiya. A disk-type apparatus for applying fluid shear-stress on cultured endothelial-cell. *Biorheology* 25:461–470, 1988.

[75]Paul, R., P. Heil, J. P. Spatz, and U. S. Schwarz. Propagation of mechanical stress through the actin cytoskeleton toward focal adhesions: model and experiment. *Biophys. J.* 94:1470–1482, 2008.

[76]Pawar, P., S. Jadhav, C. D. Eggleton, and K. Konstantopoulos. Roles of cell and microvillus deformation and

receptor–ligand binding kinetics in cell rolling. *Am. J. Physiol. Heart Circ. Physiol.* 295:H1439–H1450, 2008.

[77]Peskin, C. S., G. M. Odell, and G. F. Oster. Cellular motions and thermal fluctuations: the Brownian ratchet. *Biophys. J.* 65:316–324, 1993.

[78]Phillips, J. C., R. Braun, W. Wang, J. Gumbart, E. Tajkhorshid, *et al.* Scalable molecular dynamics with NAMD. *J. Comput. Chem.* 26:1781–1802, 2005.

[79]Pollard, T. D., and G. G. Borisy. Cellular motility driven by assembly and disassembly of actin filaments. *Cell* 112:453–465, 2003.

[80]Poujade, M., E. Grasland-Mongrain, A. Hertzog, J. Jouanneau, P. Chavrier, *et al.* Collective migration of an epithelial monolayer in response to a model wound. *Proc. Natl Acad. Sci. USA* 104:15988–15993, 2007.

[81]Rubinstein, B., K. Jacobson, and A. Mogilner. Multiscale two-dimensional modeling of a motile simple-shaped cell. *Multiscale Model. Sim.* 3:413–439, 2005.

[82]Sakamoto, N., N. Saito, X. B. Han, T. Ohashi, and M. Sato. Effect of spatial gradient in fluid shear stress on morphological changes in endothelial cells in response to flow. *Biochem. Biophys. Res. Commun.* 395:264–269, 2010.

[83]Sasamoto, A., M. Nagino, S. Kobayashi, K. Naruse, Y. Nimura, *et al.* Mechanotransduction by integrin is essential for IL-6 secretion from endothelial cells in response to uniaxial continuous stretch. *Am. J. Physiol. Cell Physiol.* 288:C1012–C1022, 2005.

[84]Sato, M., K. Nagayama, N. Kataoka, M. Sasaki, and K. Hane. Local mechanical properties measured by atomic force microscopy for cultured bovine endothelial cells exposed to shear stress. *J. Biomech.* 33:127–135, 2000.

[85]Sawada, Y., M. Tamada, B. J. Dubin-Thaler, O. Cherniavskaya, R. Sakai, *et al.* Force sensing by mechanical extension of the Src family kinase substrate p130Cas. *Cell* 127:1015–1026, 2006.

[86]Shrader, C. D., H. G. Ressetar, J. Luo, E. V. Cilento, and F. D. Reilly. Acute stretch promotes endothelial cell proliferation in wounded healing mouse skin. *Arch. Dermatol. Res.* 300:495–504, 2008.

[87]Small, J. V., M. Herzog, and K. Anderson. Actin filament organization in the fish keratocyte lamellipodium. *J. Cell Biol.* 129:1275–1286, 1995.

[88]Sun, G. Y., Y. Zhang, B. Huo, and M. Long. Surface-bound selectin–ligand binding is regulated by carrier diffusion. *Eur. Biophys. J.* 38:701–711, 2009.

[89]Szymanski, M. P., E. Metaxa, H. Meng, and J. Kolega. Endothelial cell layer subjected to impinging flow mimicking the apex of an arterial bifurcation. *Ann. Biomed. Eng.* 36:1681–1689, 2008.

[90]Ter-Oganessian, N., B. Quinn, D. A. Pink, and A. Boulbitch. Active microrheology of networks composed of semiflexible polymers: computer simulation of magnetic tweezers. *Phys. Rev. E* 72:041510, 2005.

[91]Thery, M., A. Jimenez-Dalmaroni, V. Racine, M. Bornens, and F. Julicher. Experimental and theoretical study of mitotic spindle orientation. *Nature* 447:493–496, 2007.

[92]Thery, M., V. Racine, A. Pepin, M. Piel, Y. Chen, *et al.* The extracellular matrix guides the orientation of the cell division axis. *Nat. Cell Biol.* 7:947–953, 2005.

[93]Ueki, Y., N. Sakamoto, and M. Sato. Direct measurement of shear strain in adherent vascular endothelial cells exposed to fluid shear stress. *Biochem. Biophys. Res. Commun.* 394:94–99, 2010.

[94]Ueki, Y., N. Sakamoto, and M. Sato. Cyclic force applied to focal adhesions induces actin recruitment depending on the dynamic loading pattern. *Open Biomed. Eng. J.* 4:129–134, 2010.

[95]Usami, S., H. H. Chen, Y. Zhao, S. Chien, and R. Skalak. Design and construction of a linear shear stress flow chamber. *Ann. Biomed. Eng.* 21:77–83, 1993.

[96]Verkhovsky, A. B., T. M. Svitkina, and G. G. Borisy. Network contraction model for cell translocation and retrograde flow. *Biochem. Soc. Symp.* 65:207–222, 1999.

[97]Vicente-Manzanares, M., X. Ma, R. S. Adelstein, and A. R. Horwitz. Non-muscle myosin II takes centre stage in cell adhesion and migration. *Nat. Rev. Mol. Cell Biol.* 10:778–790, 2009.

[98]Wang, G. M., and W. C. Sandberg. Complete all-atom hydrodynamics of protein unfolding in uniform flow. *Nanotechnology* 21:235101, 2010.

[99]Wang, N., and Z. Suo. Long-distance propagation of forces in a cell. *Biochem. Biophys. Res. Commun.* 328:1133–1138, 2005.

[100]Wu, J. H., Y. Fang, V. I. Zarnitsyna, T. P. Tolentino, M. L. Dustin, *et al.* A coupled diffusion-kinetics model for analysis of contact-area FRAP experiment. *Biophys. J.* 95:910–919, 2008.

[101]Wu, L., B. T. Xiao, X. L. Jia, Y. Zhang, S. Q. Lü, *et al.* Impact of carrier stiffness and microtopology on two-dimensional kinetics of P-selectin and P-selectin glycoprotein ligand-1 (PSGL-1) interactions. *J. Biol. Chem.* 282:9846–9854, 2007.

[102]Wuang, S. C., B. Ladoux, and C. T. Lim. Probing the chemo-mechanical effects of an anti-cancer drug emodin on breast cancer cells. *Mol. Cell Bioeng.*, 2011. doi: 10.1007/s12195-011-0163-1.

[103]Yago, T., J. Z. Lou, T. Wu, J. Yang, J. J. Miner, *et al.* Platelet glycoprotein Ibalpha forms catch bonds with human WT vWF but not with type 2B von Willebrand disease vWF. *J. Clin. Invest.* 118:3195–3207, 2008.

[104]Yam, P. T., C. A. Wilson, L. Ji, B. Hebert, E. L. Barnhart, *et al.* Actin–myosin network reorganization breaks symmetry at the cell rear to spontaneously initiate polarized cell motility. *J. Cell Biol.* 178:1207–1221, 2007.

[105]Yu, Y., and J. Y. Shao. Simultaneous tether extraction contributes to neutrophil rolling stabilization: a model study. *Biophys. J.* 92:418–429, 2007.

[106]Zarbock, A., and K. Ley. Mechanisms and consequences of neutrophil interaction with the endothelium. *Am. J. Pathol.* 172:1–7, 2008.

[107]Zhang, F., W. D. Marcus, N. H. Goyal, P. Selvaraj, T. A. Springer, *et al.* Two-dimensional kinetics regulation of alpha(L)beta(2)-ICAM-1 interaction by conformational changes of the alpha(L)-inserted domain. *J. Biol. Chem.* 280:42207–42218, 2005.

[108]Zhao, Y. H., S. Chien, and S. Weinbaum. Dynamic contact forces on leukocyte microvilli and their penetration of the endothelial glycocalyx. *Biophys. J.* 80:1124–1140, 2001.

[109]Zou, X., Y. Liu, Z. Chen, G. I. Cardenas-Jiron, and K. Schulten. Flow-induced beta-hairpin folding of the glycoprotein Ibalpha beta-switch. *Biophys. J.* 99:1182–1191, 2010.

In vivo imaging of the molecular distribution of the VEGF receptor during angiogenesis in a mouse model of ischemia

Yoh Hamada,[1,2] Kohsuke Gonda,[1] Motohiro Takeda,[1] Akira Sato,[2] Mika Watanabe,[3] Tomoyuki Yambe,[4] Susumu Satomi,[2] and Noriaki Ohuchi[1,5]

[1]Department of Nano-Medical Science, Graduate School of Medicine, Tohoku University, Sendai, Japan; [2]Department of Advanced Surgical Science and Technology, Graduate School of Medicine, Tohoku University, Sendai, Japan; [3]Department of Pathology, Tohoku University Hospital, Sendai, Japan; [4]Department of Medical Engineering and Cardiology, Institute of Development, Aging and Cancer, Tohoku University, Sendai, Japan; and [5]Department of Surgical Oncology, Graduate School of Medicine, Tohoku University, Sendai, Japan

Vascular endothelial growth factor (VEGF) plays a critical role in angiogenesis and has been applied to medical therapy. However, because vascular imaging at the molecular level is impossible, the detailed in vivo dynamics of VEGF and its receptor (VEGFR) remain unknown. In this study, to understand the molecular distribution of VEGF and the VEGFR, we prepared ischemic mice with a new surgical method and induced angiogenesis in the gastrocnemius muscle. Then, we made a VEGF-conjugated fluorescence nanoparticle and performed staining of VEGFR-expressing cells with the fluorescent probe, demonstrating the high affinity of the probe for VEGFR. To observe the physiologic molecular distribution of VEGFR, we performed in vivo single-particle imaging of gastrocnemius in the ischemic leg with the fluorescent probe. The results suggested that only a 3-fold difference of VEGFR distribution is involved in the formation of branched vasculature in angiogenesis, although previous ex vivo data showed a 13-fold difference in its distribution, indicating that a method inducing a several-fold local increase of VEGFR concentration may be effective in generating site-specific angiogenesis in ischemic disease. This new in vivo imaging of ischemic mice could make useful contributions to understanding the mechanisms of angiogenesis and to developing a VEGFR-related drug. (*Blood.* 2011;118(13): e93-e100)

Introduction

Angiogenesis and arteriogenesis play a critical role in neovascularization in adults.[1] Angiogenesis is defined as the sprouting of new capillaries from postcapillary venules,[2] whereas arteriogenesis is defined as the process of artery maturation or the de novo growth of collateral conduits.[3] Our laboratory studies the mechanisms of angiogenesis, and clarification of these mechanisms is crucial for the development of new treatments for arteriosclerotic disorders. Recently, medical applications for recombinant vascular endothelial growth factor (VEGF) proteins or genes have been developed.[4] However, no placebo-controlled trial has yielded overwhelmingly positive results.[1] An understanding of the detailed molecular mechanisms of this angiogenesis factor in vivo is thought to be very important for the effective design of a VEGF-related drug delivery system. However, neither VEGF activity nor VEGFR distribution has been quantitatively analyzed in vivo at a molecular level with respect to therapeutic angiogenesis. In previous animal studies, the efficacy of treatment for atherosclerotic disease was primarily evaluated using angiography, laser Doppler imaging, and the determination of histologic capillary density.[5,6] Angiography can be used to noninvasively visualize vessel size, vessel branching, and the vascular network throughout the body. However, because it is difficult to visualize vascular structures several hundred micrometers beneath the imaging surface, this method is not adequate for the observation of early-stage angiogenesis at a

molecular level. Laser Doppler imaging provides a noninvasive measurement of blood flow by determining the Doppler frequency shift of reflected light because of the motion of red blood cells. This technique enables quantitative analysis of improvements in blood flow after injury to the vasculature. However, the Doppler shift measurement is easily influenced by movement artifacts, room temperature, and blood pressure.[7] In addition, it is difficult to analyze microvascular structures using laser Doppler imaging because the resolution of the obtained image is limited by diffusion of the reflected light because of distance between the red blood cells and the detector. Histologic measurements of capillary density can reveal quantitative increases in blood vessel density, and many previous studies have used this metric as a standard evaluation of angiogenesis. However, continuous observation of the same tissue is impossible with this measurement technique as protein structure is influenced by fixation of the tissues. For this reason, histologic techniques are not recommended for physiologic observations of the angiogenesis process. In the aforementioned methods, as resolution is limited to the micrometer level and imaging at the molecular level is currently impossible, the detailed in vivo dynamics of individual VEGF and VEGF receptor (VEGFR) molecules remain unknown. We have developed an in vivo single-particle imaging system using bright and photo-stable fluorescent nanoparticles, or quantum dots (QDs), with a spatial
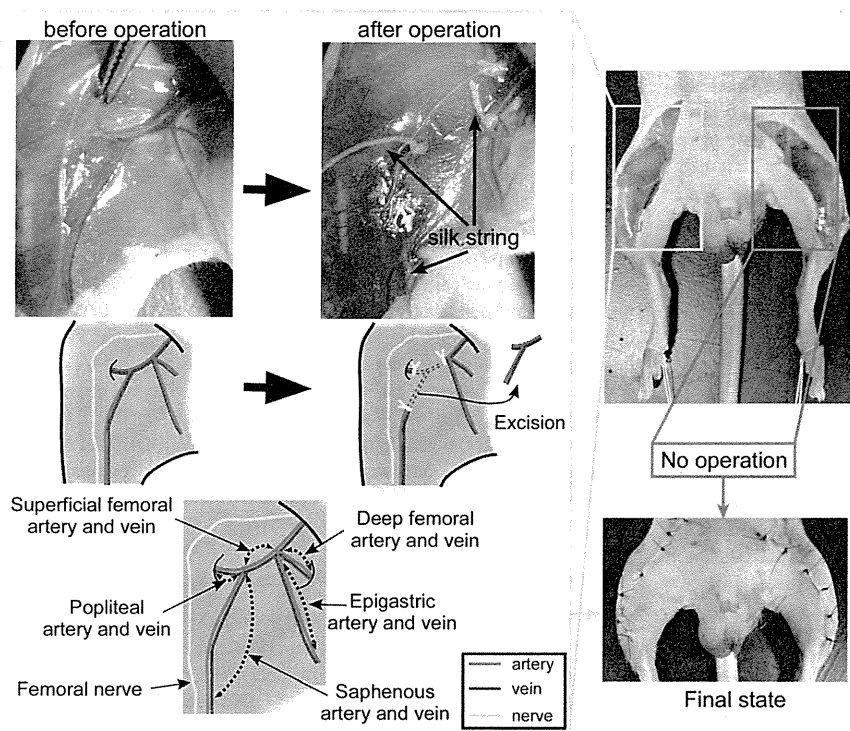
Figure 1. Procedure for preparing the hemi-hind limb ischemic mouse model. On the right leg, we ligated the proximal end of the superficial femoral artery and vein, the origins of the popliteal artery and vein, and the distal portions of the saphenous artery and vein with surgical silk. All vessels surrounding the 3 ligated points were excised. The left leg was not treated, except for an incision in the skin of the thigh.

precision of 7-9 nm. This was performed to clarify the molecular mechanisms of an anti-HER2 antibody-based drug delivery system and of cancer metastasis in tumor-bearing mice.[8,9]

The use of an ischemic mouse model is highly effective for understanding the in vivo molecular dynamics of angiogenic factors and their effects on vascular remodeling. However, 2 surgical concerns impose limitations on previous mouse models.[10] First, angiogenesis and arteriogenesis were not separately evaluated in previous models. As both processes contribute to an increase in the rate of blood flow,[1] it is necessary that the effects of arteriogenesis be eliminated if angiogenesis is to be analyzed. Second, inflammation and edema at the surgical site are known to affect angiogenesis.[11] To overcome these problems, it is critical to establish an improved ischemic mouse model that selectively induces angiogenesis at a specific muscle. Here, we demonstrate the development of an imaging method for determining the molecular distribution of VEGFR labeled with QD-conjugated VEGF. This technique was designed to observe angiogenesis in a novel ischemic mouse model that induces angiogenesis in the gastrocnemius. Our results suggest that only a several-fold difference in VEGFR distribution is required for the promotion of angiogenesis. This novel imaging method may aid in the development of drugs and treatments for atherosclerotic diseases.

Methods

Animals

C57BL/6J male mice (Charles River Laboratories) weighing 20-27 g and 8-9 weeks of age were used for all experiments. All surgical processes were performed under anesthesia with ketamine (100-120 mg/kg) and xylazine (8-10 mg/kg). Anesthesia was maintained for the course of the imaging session. Animals were used in accordance with guidelines approved by the committee on animal experiments of Tohoku University.

Hemi-hind limb ischemic mouse model

The hair of each mouse was removed from the abdomen and both hind limbs with an electric shaver and depilatory cream. The skin from both thighs was then incised to expose the arteries, veins, and nerves. To induce selective ischemia in the gastrocnemius, which is located in the deep layer of the thigh muscles, 3 vessels of the femoral area were ligated in the right hind limb. First, the proximal end of the superficial femoral artery and vein were ligated with surgical silk, size 6-0. Second, the origins of the popliteal artery and vein were ligated. Third, the distal portions of the saphenous artery and vein were ligated to avoid the backflow of blood. Femoral nerves were carefully preserved. Each of the vessels that were surrounded by the 3 ligated points was excised. The left leg was not treated, except for an incision in the skin of the thigh. Finally, the overlying skin was closed (Figure 1).

Histologic capillary density

To confirm that the surgical operation-induced angiogenesis in the gastrocnemius, we performed immunohistologic staining of the muscle with anti-CD31 antibody, a marker for vascular endothelial cells. Mice were killed at predetermined times (7, 14, 21, and 28 days after operation). The gastrocnemius was removed and fixed overnight in 10% formalin in PBS. After fixation, the tissue was embedded in paraffin, and the tissue sections were prepared and mounted on slides. The tissue samples were deparaffinized, and antigen retrieval was performed with proteinase K treatment. After this treatment, the tissue samples were incubated with a rat anti-CD31 monoclonal primary antibody (Angio-Proteomie) at 5 μg/mL for 12 hours at 4°C. After being washed with PBS, the samples were incubated with a biotinylated antirat IgG secondary antibody (Vector Laboratories; 100-fold dilution) for 30 minutes at 25°C. After incubation, the samples were incubated with HRP-conjugated streptavidin (Nidchirei) for 30 minutes at 25°C. Samples were then treated with diaminobenzidine chromogen reagent (Dojindo) and counterstained with hematoxylin. The samples were observed using light microscopy (BX51; Olympus) with an objective lens (×40, 0.75 NA; Olympus) and a camera (DP-25B; Olympus). The images were acquired with image processing software (DP2-BSW Version 1.2).

Laser Doppler perfusion imaging

Blood perfusion of the hind limb was measured using a Laser Doppler Perfusion Imaging system (MoorLDI2-IR; Moor Instruments). This imaging technique provides a noninvasive measurement of blood flow by determining the Doppler frequency shift of light reflected off of moving red blood cells. Mice under the same anesthetic dose described in "Animals" were scanned from the lower abdomen to the end of the toes. After scanning, colored images were obtained with original software (RE-SEARCH Version 3.09; Moor Instruments). Each pixel in the acquired images reflected an original blood flow value, referred to as a perfusion unit (PU). The mean of the PUs of the lower thighs in a control limb and a treated hind limb was determined. The PUs of ischemic legs were obtained at different time points (before operation, soon after operation, and 7, 14, 21, and 28 days after operation). The relative ratios of the mean PUs between the ischemic and control legs in the same mouse were calculated.

Cell lines

A pancreatic islet endothelial mouse cell line, MS1, was obtained from ATCC. MS1-VEGF cells, which express VEGFR on the cell membrane via the transfection of the VEGF gene, were also acquired from ATCC. These cells were cultured in DMEM (Invitrogen) supplemented with 5% FBS.

Immunostaining of cultured cells with an anti-VEGFR antibody

MS1 and MS1-VEGF cells were cultured on slide glass chambers. After 3 days, the slides were placed in 2.5% formalin in DMEM for 10 minutes. After fixation, the cells were incubated with an anti–mouse VEGFR monoclonal antibody (Pierce Chemical) or a whole mouse IgG (Rockland) primary antibody at 10 μg/mL for 12 hours at 25°C. After the samples were washed with PBS, the cells were incubated with a HRP-conjugated anti–mouse IgG secondary antibody (KPL Europe; 100-fold dilution) for 1 hour at 25°C. After incubation, the samples were treated with diaminobenzidine chromogen reagent and counterstained with hematoxylin. We observed the samples with the same optical system in "Histologic capillary density."

Preparation of angiogenesis factor-conjugated QDs

Mouse VEGF 164 (R&D Systems) and platelet-derived growth factor BB (PDGF; Biovision) were biotinylated using the EZ-Link Micro Sulfo-NHS-LC-Biotinylation Kit (Pierce Chemical). In this reaction, a 1:50 molar ratio of angiogenesis factors and Sulfo-NHS-LC-Biotin was used according to the manufacturer's instructions. The biotinylated VEGF and PDGF were then mixed with avidin-conjugated Qdot705 nanoparticles (QD705; Invitrogen) at a molar ratio of 8:1 or 16:1 and incubated for 1 hour at 25°C. The number of QD705 nanoparticles determined the emission wavelength. QD705-conjugated VEGF and PDGF were termed VEGF-QD and PDGF-QD, respectively.

Single-particle imaging system

The optical system used to observe the fluorescence of the angiogenesis factor-conjugated QDs consisted primarily of an epifluorescent microscope (IX-71; Olympus), a Nipkow disk-type confocal unit (CSU10; Yokogawa), and an EMCCD camera (Ixon DV887; Andor). An objective lens (60×, PlanApo, 1.40 NA; Olympus) was used for imaging. VEGF-QDs were illuminated using a green laser (532 nm; Spectra-Physics). The laser-excited fluorescence of the QDs was filtered with a 695- to 740-nm band-pass filter. Images were obtained at a rate of 5 frames/second. For in vivo imaging, to remove the oscillation because of heartbeats and respiration, a gastrocnemius window was developed and attached to the aforementioned microscopy system.

Single-particle imaging of VEGF-QDs in cultured cells

To investigate the affinity of VEGF-QDs for VEGFR, MS1, and MS1-VEGF, cells were incubated with 1, 10, or 50nM VEGF-QDs for 1 hour at 25°C. After 3 washes with DMEM, these cells were observed in a glass-bottom dish using the single-particle imaging system. The fluores-

cence intensities of QD signals from the cells were analyzed as gray values using ImageJ 1.38 software (www.rsb.info.nih.gov/ij). The gray values of 100 frames (200 milliseconds/frame) from a single cell were averaged, and the gray value of the background was subtracted from that of the cell. The mean gray value per pixel in the background-subtracted image of the cell was multiplied by the total number of pixels making up the image of the cell. The total fluorescence intensity of the QDs per cell was thus determined. In the 10nM VEGF-QD treatment, QD fluorescence signals were clearly observed on MS1-VEGF cells. In contrast, when MS1-VEGF cells were incubated with 1nM VEGF-QDs, the QD fluorescence signals were low. When the cells were treated with 50nM VEGF-QDs, QD signals were exceedingly high or even saturated (data not shown). In MS1 cells incubated with various concentrations of VEGF-QDs, the VEGF-QD fluorescence signals were very low. These results indicate that VEGF-QDs specifically recognize VEGFR and that the 10nM concentration was appropriate for imaging the binding of VEGF-QDs to VEGFR. Moreover, to provide stronger evidence of the affinity of VEGF-QDs for VEGFR, MS1, and MS1-VEGF, cells were incubated with 10nM unconjugated QDs, PDGF-QDs, or VEGF-QDs for 1 hour at 25°C, and the resulting fluorescence intensities were examined.

In vivo fluorescence imaging with the IVIS Spectrum system

To confirm that VEGF-QDs accumulated in the ischemic leg, we performed in vivo fluorescence imaging using the IVIS Spectrum imaging system (Caliper Life Sciences) at 4, 9, and 14 days after preparation of ischemic model mice. Unconjugated QDs or VEGF-QDs were injected intracardially into the mice. The final concentration of the QD probes in the blood was 10nM, as determined by the single-particle imaging data from cultured cells. The detection sensitivity of the fluorescent signal using the IVIS Spectrum is poorer than the single-particle imaging system but allows for noninvasive visualization of the whole body of the mouse. Therefore, fluorescence images were taken 10 minutes after injection of fluorescent probes, before the fluorescence signals decreased, because of their washing out with the blood. Fluorescence intensities of the QDs were analyzed using accessory software (Living Image Version 4.0; Caliper Life Sciences). For data analyses, the relative ratio of fluorescence between the ischemic and control leg of the same mouse was calculated.

Single-particle imaging of VEGF-QDs in the gastrocnemius of ischemic model mice

To examine the distribution of VEGF-QDs in the gastrocnemius of the ischemic leg, we performed in vivo single-particle imaging of the vasculature 4, 9, and 14 days after operation. The skin of the ischemic leg was opened to expose the thigh muscles. The skin of the hind limbs was then fixed to a plastic plate using suture thread and Superglue. Use of Superglue made both connections of the skin to the plate more stable without damaging the vasculature, eliminating the background oscillations from the heartbeat and respiration during observation. To expose the gastrocnemius, the skin and hemimembranous muscle, which is located on the superficial layer of the gastrocnemius, were then removed. The mouse, which was mounted as described on the plastic plate, was then fixed to a hand-made aluminum stage designed to stabilize the plate with screws. Unconjugated QDs or VEGF-QDs were injected intracardially into the mice. The sensitivity of the single-particle imaging system to the fluorescence signal is extremely high; and immediately after injection, a part of probes are free in the blood and have not bound to VEGFR. This initially prevents observation of the interaction between the VEGF-QDs and VEGFR on the vascular wall. Therefore, in vivo single-particle imaging of the fluorescent probes was carried out 1 hour after injection. By this time, the concentration of the free probe in the blood was decreased. To quantitatively measure the affinity of the VEGF-QDs for the vasculature, an analysis was performed as follows. A total of 100 frames, each 512 pixels square and representing an exposure of 200 milliseconds, were overlaid using image processing software (G-count 1.01; G-angstrom). A portion of the overlaid (192 pixels square) image was examined to determine the number of QD particles in proper-sized vasculature. For each image analyzed, the fluorescence intensity (as gray values) of QD signals from the tissues was determined using ImageJ software. The mean gray value, derived from the tissues'
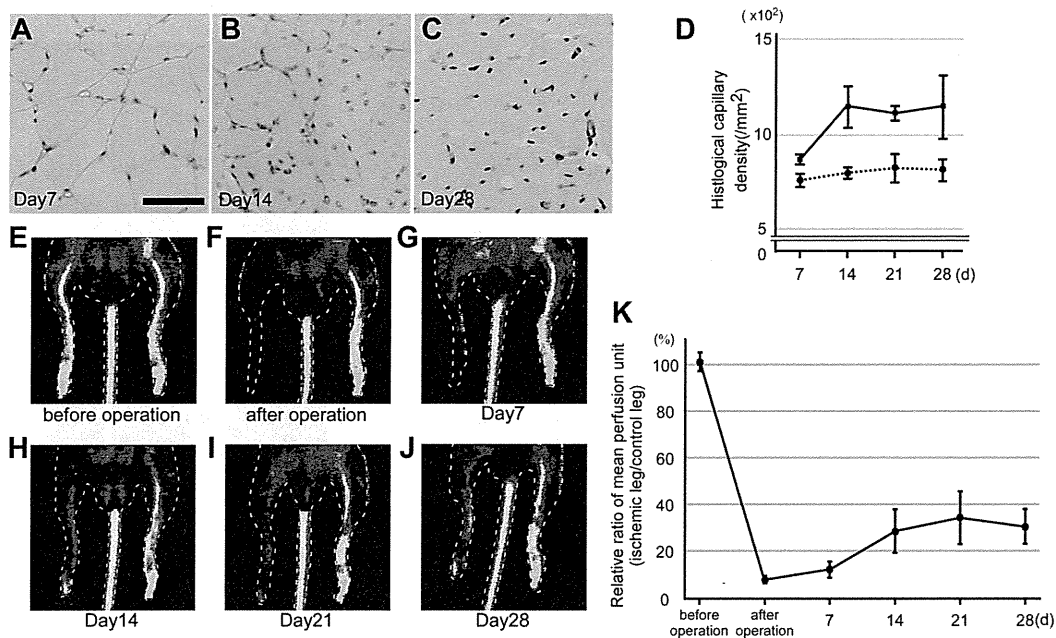
Figure 2. Evaluation of angiogenesis of the ischemic model mice. (A-C) Typical images of the gastrocnemius immunostained with an anti-CD31 antibody. The muscles from ischemic legs were isolated at 7, 14, and 28 days after the induction of ischemia and immunostained. Brown circles and dots represent CD31+ capillaries. Scale bar represents 50 μm. (D) Measurement of CD31+ capillary density. In the gastrocnemius of the ischemic or control leg, capillaries stained with the anti-CD31 antibody were counted. Solid and dotted lines represent the sample derived from ischemic and control legs, respectively. n = 4. Error bars represent SEM. (E-J) Changes in blood perfusion were assessed using laser Doppler perfusion imaging in ischemic legs of model mice. (E-F) Images before and soon after operation. After operation, the perfusion signal in the ischemic leg is significantly decreased. (G-J) Images from 7, 14, 21, and 28 days after operation. Blood perfusion in an ischemic leg gradually increases. (K) Change in perfusion units as determined by this imaging technique. Relative ratios of mean perfusion units between ischemic and control legs in the same mouse are shown (ischemic leg value/control leg value). n = 6. Error bars represent SEM.

autofluorescence per pixel, was subtracted from the fluorescence value of the vascular wall area. The resulting gray value was then multiplied by the total number of pixels of the vascular wall. This value reflected the total fluorescence intensity of all QDs bound to the vascular wall (total QD value).

To precisely determine the number of QD particles on the vascular wall, it was necessary to define the fluorescence intensity of a single QD. Because QDs that fluoresce at the same wavelength are uniform in size, QD705 fluorescence intensity is proportional to the particle number. Moreover, the QD fluorescence is composed of fluorescent and nonfluorescent states referred to as on- and off-states. This property results in blinking of a QD. When the fluorescence and other properties of QD particles were analyzed immediately after their purchase, we determined that the mean duration of the off-state over 20 seconds was approximately 4 seconds and that the calculated SEM was very low.[12] In cases where QDs aggregate, the mean duration of the off-state per unit time is shortened because the on- and off-states of each particle in the aggregate occur randomly. Therefore, based on an off-state duration of 4 seconds, we selected a single particle QD from each image and measured the fluorescence intensity of the single QD particle (single QD value) in the same manner as the total QD value. The total QD value was divided by a single QD value, and the number of QD particles per 10 μm of vascular wall was calculated.

Statistical analysis

Data are mean ± SEM. An F test was performed and equal variance was defined as P values ≥ .05. Comparisons between groups were performed using the parametric Student t test (≥ .05 at F test) or Welch t test ($P < .05$ at F test). $P < .05$ was considered significant for both t tests.

Results

Induction of angiogenesis in ischemic model mice

To induce angiogenesis at a selected site and to eliminate the effects of inflammation and edema,[11] we targeted the gastrocnemius. This muscle is primarily supplied by the popliteal and saphenous arteries, and no remarkable collateral arteries exist near the muscle. We therefore ligated the popliteal and saphenous arteries to induce angiogenesis in the gastrocnemius (Figure 1). Other muscles in the thigh are primarily supplied by the deep femoral artery, which was maintained as a collateral artery after the surgery. Therefore, we think that our surgery is appropriate for analyses of angiogenesis mechanisms. The gastrocnemius is located deep among the thigh muscles, and the skin and semimembranosus muscle located on the upper layer of the gastrocnemius were removed just before in vivo imaging. Therefore, we avoided the effects of inflammation and edema-induced factors on normal angiogenesis. To determine whether the number of capillaries in the gastrocnemius of ischemic legs increased, we histologically determined the capillary densities over time (Figure 2A-C). Capillary densities in the control legs did not significantly change during observation (Figure 2D). In contrast, the capillary densities in ischemic legs increased gradually over 14 days, peaked at day 14, and were steady between day 14 and day 28. This finding demonstrates that angiogenesis was induced in the ischemic leg (Figure 2D). To investigate improvement of blood flow in the model mice using another method, we evaluated the change in blood flow using laser Doppler perfusion imaging (Figure 2E-J). The relative ratio of the mean PU between ischemic and control legs in the same mouse (ischemic leg value/control leg value) decreased to ~ 8% soon after operation (Figure 2E-F,K). This ratio then increased to ~ 34% 21 days after the surgery (Figure 2I,K). Both observations indicate that angiogenesis was effectively induced in the gastrocnemius between 7 days and 14 days after the procedure. The slight difference in the rate of increase of perfusion between the 2 imaging methods may be because the laser Doppler perfusion imaging analyzed the thigh as a whole, and arteriogenesis induced by inflammation and

Figure 3. VEGFR distribution in MS1 and MS1-VEGF cells and the affinity of angiogenesis factor-conjugated QDs to these cell lines. (A-D) Immunostaining of MS1 and MS1-VEGF cells with an anti-VEGFR antibody. Scale bar represents 50 μm. (E-H) Typical images of cells treated with fluorescent particles. MS1 and MS1-VEGF cells were treated with unconjugated QDs, PDGF-QDs, or VEGF-QDs. Representative images are shown of cells treated with PDGF-QDs and VEGF-QDs. Data from cells treated with unconjugated QDs are not shown. White dots represent fluorescent QDs; and white dotted lines, the outline of the cell. Scale bar represents 10 μm. (I) QD fluorescence intensity per cell. The fluorescence intensity of QD signals from the cells was analyzed as gray values. In each condition, n = 30. **P < .01. Error bars represent SEM.
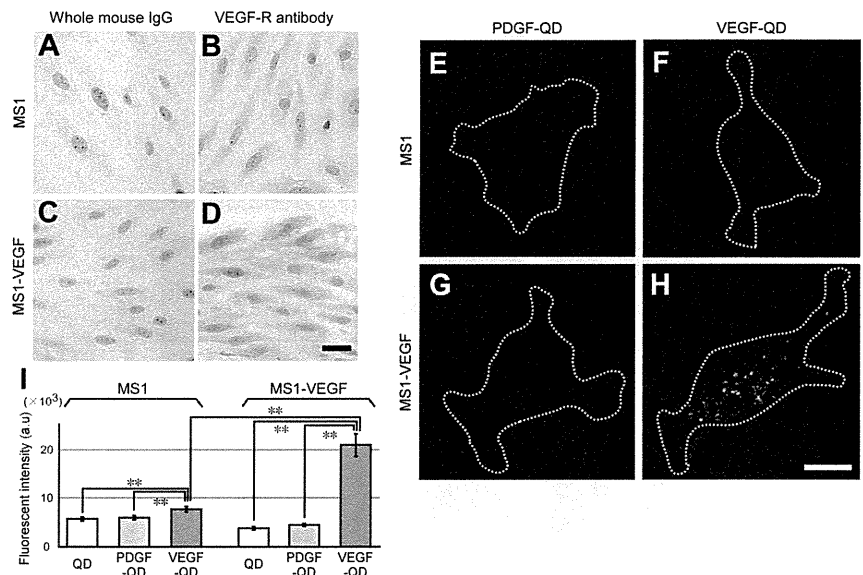
edema of the semimembranous muscle may have occurred in this larger volume.

Preparation and characterization of VEGF-QDs

To visualize the molecular distribution of VEGF using single-particle imaging, VEGF was conjugated with QDs (VEGF-QD). PDGF-conjugated QDs (PDGF-QD) were also prepared as control probes (supplemental Figure 1, available on the *Blood* Web site; see the Supplemental Materials link at the top of the online article). To examine the binding of VEGF-QD and VEGFR, staining was performed on MS1 and MS1-VEGF cells treated with unconjugated QDs, PDGF-QDs, and VEGF-QDs. High levels of VEGFR expression in MS1-VEGF cells were confirmed by immunostaining with an anti-VEGFR antibody (Figure 3C-D), whereas low-level expression was observed in MS1 cells (Figure 3A-B). The analyses of QD-probe fluorescence indicated that the total fluorescence intensity of VEGF-QDs in MS1-VEGF cells was $21.0 \pm 2.4 \times 10^4$ (Figure 3H-I). This value was remarkably higher than the observed fluorescence values of stained MS1-VEGF cells treated with unconjugated QDs or PDGF-QDs (unconjugated QDs, $3.8 \pm 0.3 \times 10^4$; PDGF-QDs, $4.4 \pm 0.3 \times 10^4$; Figure 3G,I) and those of MS1 cells treated with unconjugated QDs, PDGF-QDs, or VEGF-QDs (unconjugated QDs, $5.7 \pm 0.4 \times 10^4$; PDGF-QDs, $6.0 \pm 0.4 \times 10^4$; VEGF-QDs, $7.7 \pm 0.6 \times 10^4$; Figure 3E-F,I). These results demonstrate that VEGF-QDs bind specifically to VEGFR.

In vivo distribution of VEGFR labeled with VEGF-QDs

To determine the distribution of VEGFR labeled with VEGF-QDs during angiogenesis, we performed 2 in vivo fluorescence imaging techniques. In these imaging protocols, we examined ischemic model mice at 4, 9, and 14 days after operation to analyze in detail the changes in VEGFR distribution over time. Imaging performed with the IVIS Spectrum system has the advantage of imaging the fluorescence of the entire body of the mouse, although the spatial precision of this technique is low. To simultaneously observe the fluorescence of both ischemic and control legs after injection of unconjugated QDs or VEGF-QDs into the model mice, the IVIS Spectrum system was used (Figure 4A-D). Individual mice exhibit different degrees of autofluorescence. The relative ratio of fluores-

cence between the ischemic and control leg in each mouse was therefore calculated (ischemic leg fluorescence/control leg fluorescence). In model mice at 4 days after operation, the relative fluorescence ratio resulting from injection of unconjugated QDs was 0.71 ± 0.01, and the ratio after injection of VEGF-QDs was 0.72 ± 0.03 (Figure 4E). These results indicate that VEGF-QDs did not selectively accumulate in the ischemic legs at the time of
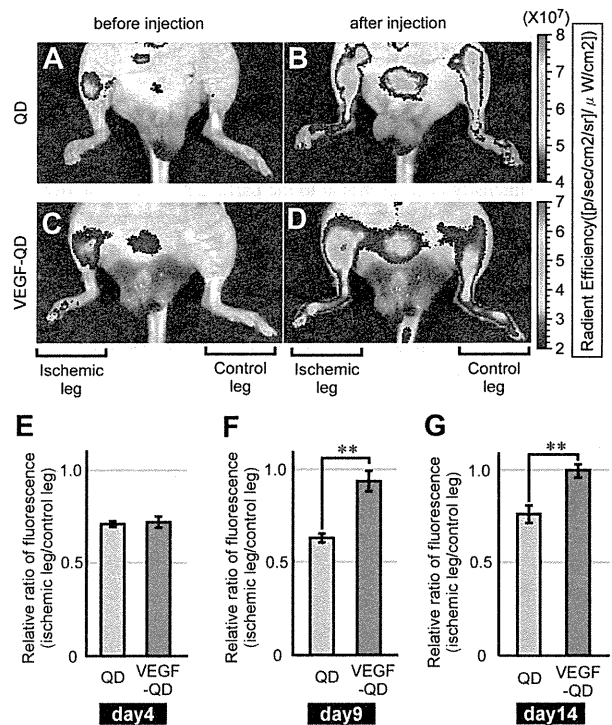

Figure 4. In vivo fluorescence imaging of the ischemic model mice using the IVIS Spectrum system. (A-D) Images using IVIS Spectrum. Unconjugated QDs and VEGF-QDs were injected intracardially into the model mice. Mice were illuminated with light with a wavelength of 625-655 nm. Excited fluorescence was filtered with a 690- to 710-nm wavelength band-pass filter. (E-G) The relative ratios of fluorescence between ischemic and control legs in mice at 4 days (E), 9 days (F), and 14 days (G) after operation. The fluorescence intensity of the ischemic leg divided by that of the control leg was calculated (ischemic leg fluorescence/control leg fluorescence). n = 5. Error bars represent SEM. **P < .05.
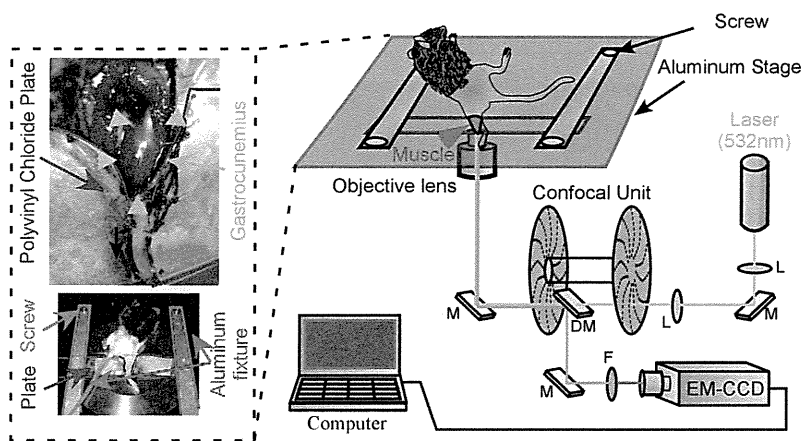
Figure 5. Schematic of the in vivo single-particle imaging system. An ischemic leg of a model mouse was stabilized on a polyvinyl plate using suture thread and instant Superglue. The skin and hemimembranous muscle were then removed. The gastrocnemius was selectively imaged using a single-particle imaging system.

measurement. In contrast, at 9 and 14 days after operation, the relative ratios resulting from injection of unconjugated QDs were 0.65 ± 0.02 and 0.76 ± 0.05, respectively, whereas the observed ratios after injection of VEGF-QDs were 0.94 ± 0.06 and 1.00 ± 0.04, respectively (Figure 4F-G), suggesting that VEGF-QDs accumulated in the ischemic leg to a greater degree than in the control leg at the time of measurement.

In addition to using the IVIS system, we also conducted in vivo single-particle imaging. For this protocol, we developed surgical fixation methods of mice beyond that in our previous imaging method. In particular, we designed a polyvinyl chloride plate with a window fit to the shape of the gastrocnemius. The skin around the gastrocnemius was bound to the plate with suture thread and Superglue (Figure 5). These improvements eliminated background oscillations because of the heartbeat and respiration, enabling us to observe the physiologic angiogenesis that sustains blood flow after ischemia (supplemental Movies 1, 2). We observed the distribution of unconjugated QDs or VEGF-QDs after injection of the respective probe. The results indicate that a large number of VEGF-QDs were specifically localized on the vessel walls in ischemic legs (Figure 6A-H), whereas fluorescence after injection of unconjugated QDs was very weak (supplemental Figure 2A-D). We measured the total fluorescence intensity resulting from all QDs on the vascular wall (total QD value) and the fluorescence intensity of single QD (single QD value) as gray values. The total QD value was then divided by the single QD value, and the number of QD particles per 10 μm of the vascular wall was calculated (Figure 6I; supplemental Figure 2E). These analyses revealed that QD fluorescence on the vascular wall was weak in both ischemic and control legs in mice injected with unconjugated QDs (supplemental Figure 2E). When VEGF-QDs probe were injected at 4 days after operation, the number of VEGF-QDs on the vascular walls of ischemic legs was similar to the number observed in control legs. Moreover, there was no difference in number of particles on the walls of branched or linear vasculature in ischemic legs (Figure 6C-D,I). In contrast, the number of VEGF-QDs in the branched vasculature in ischemic legs was 3.4-fold greater than the number of VEGF-QDs in the linear vasculature 9 days after operation (Figure 6E-F,I) and 4.5-fold greater than the number of VEGF-QDs in the branched vasculature in control legs (Figure 6B,F,I). Fourteen days after operation, the number of VEGF-QDs on the walls of the branched vasculature in ischemic legs was 3.3-fold greater than the number of particles on the walls of the linear vasculature (Figure 6G-I) and 4.3-fold greater than the number of

VEGF-QDs in the branched vasculature in control legs (Figure 6I). These results demonstrate that our single-particle imaging method is able to quantitatively describe the in vivo distribution of VEGFR labeled with VEGF-QDs during angiogenesis in ischemic legs.

Discussion

In vivo molecular imaging using high spatial precision in ischemic model mice is highly effective for the quantitative description of the molecular dynamics of VEGF and VEGFR during angiogenesis. This information can be applied to the development of treatments for ischemic disease. Previously described mouse models suffered from surgical limitations. These difficulties involved: (1) the induction of angiogenesis without arteriogenesis, an effect of arteries that remains after surgery; and (2) the induction of inflammation and edema during surgery.[10] We focused on the gastrocnemius, which is located deep in the thigh, and developed a new ischemic mouse model consisting of the ligation of 3 pairs of vessels: the superficial femoral, popliteal, and saphenous arteries and veins (Figure 1). We confirmed that angiogenesis was effectively induced in the model mice using conventional evaluation methods, histological capillary density measurements, and laser Doppler imaging (Figure 2D,K).

We have previously described the development of in vivo single-particle imaging using QDs with a spatial precision of 7-9 nm to clarify the molecular mechanisms of a anti-HER2 antibody-based drug delivery system and cancer metastasis in tumor-bearing mice.[8,9] In previous studies, in vivo imaging with high spatial precision was not applied to the visualization of angiogenesis. For this application in the current studies, we further modified our surgical fixation method (Figure 5). For the imaging technique used here, we designed a polyvinyl chloride plate with a window fit to the shape for the gastrocnemius. This window enabled us to observe the physiologic angiogenesis during active blood flow. We observed the in vivo molecular distribution of VEGF-QDs using this improved imaging in ischemic mice at 4, 9, and 14 days after a surgery in which angiogenesis in the gastrocnemius was effectively induced. The results demonstrate that a large number of VEGF-QDs specifically localized to the vessel wall in ischemic legs (Figure 6A-H), whereas fluorescence resulting from unconjugated QDs at the wall was very weak (supplemental Figure 2A-D). To quantitatively analyze the molecular distribution of VEGF-QD-labeled VEGFRs, we measured the total number of QDs
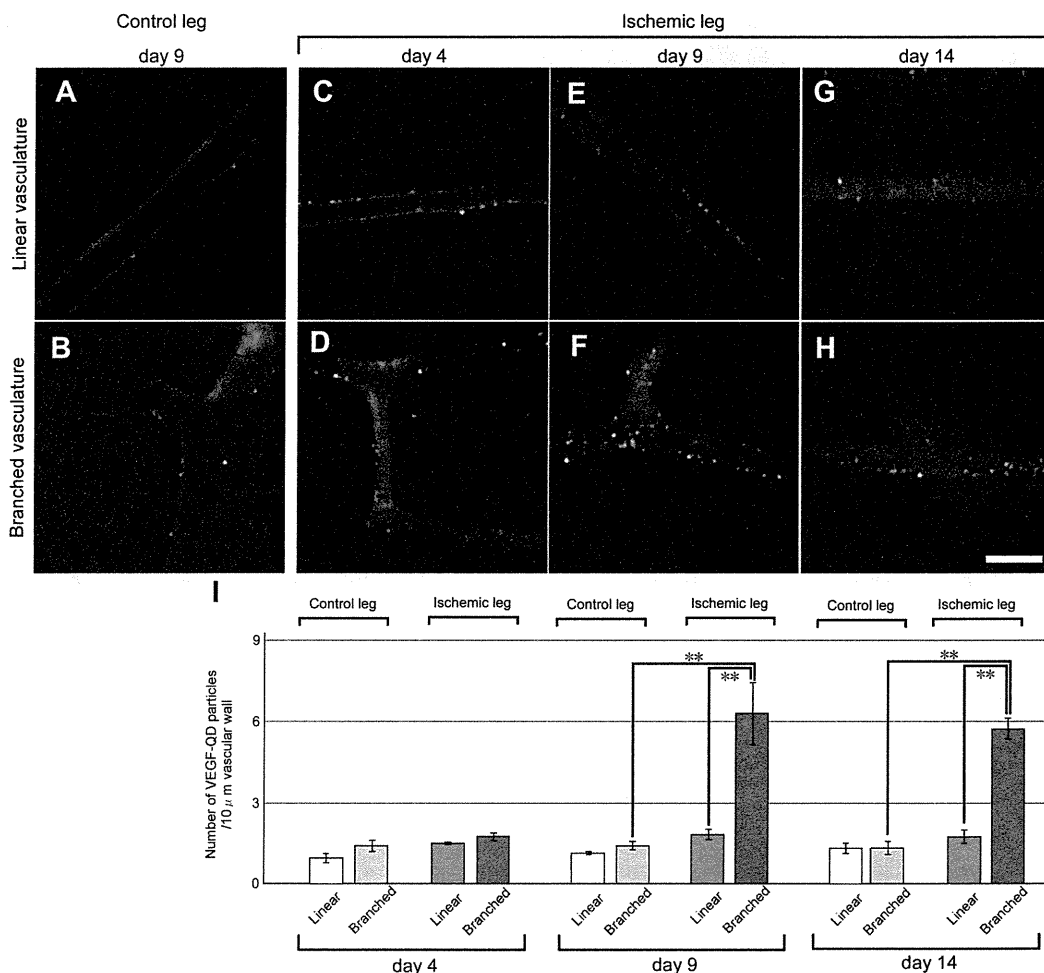
Figure 6. In vivo imaging of unconjugated and VEGF-QDs during angiogenesis in ischemic legs. (A-H) Typical images of vasculature in control and ischemic legs. These images were generated by overlaying 100 frames (200 ms/frame), each consisting of a 192-pixel square image, using Adobe after effect CS4 9.0.3 software. In model mice injected with VEGF-QDs, we observed "linear vasculature" (A,C,E,G) and "branched vasculature" (B,D,F,H) in control and ischemic mouse legs at 4, 9, and 14 days after operation. The data from unconjugated QDs are not shown (supplemental Figure 2). White dots represent QD fluorescence. Scale bar represents 10 μm. (I) The number of VEGF-QDs in different types of vasculature. The number of fluorescent particles per 10 μm of the vascular wall is quantified. n = 4. **$P < .05$. Error bars represent SEM.

(Figure 6I; supplemental Figure 2E). Because QDs with the same fluorescence wavelength are uniform in size, the fluorescence intensity of the QDs is proportional to the number of particles.[12] This property enabled us to determine relative VEGFR expression levels with a very high degree of accuracy. In mice 4 days after operation, there were no significant differences between the branched vasculature and the linear vasculature (Figure 6C-D,I). Furthermore, the IVIS Spectrum data from this time point did not show a significant difference in the accumulation of unconjugated QDs or VEGF-QDs in ischemic legs (Figure 4E). These data indicate that any VEGFR redistribution induced by hypoxic stimulation in ischemic legs occurs only at low levels at this time point. In mice at 9 days after operation, the data demonstrate a 3.4-fold greater number of VEGF-QDs on the walls of branched vasculature in ischemic legs than on the walls of linear vasculature in these legs and a 4.5-fold greater number than on the branched vasculature of control legs in model mice (Figure 6I). In mice at 14 days after operation, the data revealed that the number of VEGF-QDs on the walls of branched vasculature in ischemic legs was 3.3-fold greater than that on the linear vasculature in ischemic legs and 4.3-fold greater number than the number of VEGF-QDs on the branched vasculature in control legs in model mice (Figure 6I). These results demonstrate that the data acquired from mice at 9 and 14 days after operation using the single-particle

imaging technique were similar to data acquired using the IVIS Spectrum system (Figure 4F-G). From the data, it appears that the VEGFR protein expression on the branched vasculature in ischemic legs increases gradually between day 4 and day 9 via hypoxic stimulation, peaks at approximately day 9, and remains steady from day 9 to day 14. Histologic capillary density data reveal that capillary densities in ischemic legs increase gradually over 14 days (Figure 2D). It is very interesting, therefore, that the peak of VEGFR expression occurred ~ 9 days after the procedure. Furthermore, these data suggest that only a several-fold increase in the expression level of VEGFR on endothelial cells is critical for angiogenesis in ischemic tissues.

During angiogenesis, tip cells, stalk cells, and phalanx cells control vessel sprouting. Tip cells are located at the forefront of the sprouting vessel, stalk cells are located behind the tip cell at the branch, and phalanx cells are found in the unbranched endothelial layer.[13] Previous ex vivo studies reported that VEGFR expression in the tip cell is high to sense the VEGF concentration gradient in the extravascular area. In stalk cells, which control elongation of a new branch, VEGFR levels are lower than in the tip cells.[14] In phalanx cells, which normalize the endothelial cell layer, VEGFR levels are lower than in the stalk cells.[13] However, these are

qualitative data, and a quantitative analysis of the VEGFR distribution required to regulate the behavior of these cells has not been carried out in vivo. In addition, previous ex vivo data revealed that the amount of VEGFR protein involved in angiogenesis in ischemic tissue is 13-fold greater than in normal tissues.[15] In this report, however, because the total amount of VEGFR in both the vessel wall and the extravascular area was measured, the detailed quantitative distribution of VEGFR was not known. Our results suggest that only an approximately 3-fold difference in VEGFR distribution on the vascular wall is involved in the formation of branched vasculature from linear vasculature during angiogenesis (Figure 6I). The increase in VEGFR levels we observe after ischemia may quantitatively reveal a gradient of VEGFR expression levels between the stalk cells and pharynx cells.

Our results indicate that VEGFR distribution in in vivo ischemic tissues increased gradually over a specific period and remained steady at an approximately 3-fold increase. To increase the number of sprouting vessels for the operation of ischemic hypoxia, the steady several-fold increase of VEGFR expression levels at the ischemic site may be effective for controlled angiogenesis. Previously, treatment against ischemic hypoxia using VEGF gene therapy induced only a slight increase in VEGF blood concentrations.[16] In addition, overexpression of VEGF produces abnormal vessels in tumor angiogenesis.[17] These results suggest that in the context of ischemia, it is difficult to site-specifically modulate the concentration of a VEGF-related therapeutic to an appropriate value. Therefore, next-generation therapies targeting VEGFR, in addition to VEGF, may effectively induce site-specific angiogenesis for the treatment of ischemic disease. The novel in vivo imaging technique described here for the analysis of ischemic model mice may increase the understanding of the mechanisms of angiogenesis and aid in the development of VEGFR-related therapies.

Acknowledgments

Authorship

Contribution: Y.H. and K.G. designed and performed the research, analyzed the data, and wrote the manuscript; M.T., A.S., and N.O. performed research and analyzed data; M.W. and S.S. performed research; and T.Y. provided the equipment for laser Doppler perfusion imaging and performed research.

Conflict-of-interest disclosure: K.G. and M.T. have received a research grant from Konica Minolta Medical & Graphic Inc. N.O. has received research grants from Takeda Pharmaceutical Company Limited and Konica Minolta Medical & Graphic Inc. The remaining authors declare no competing financial interests.

Correspondence: Kohsuke Gonda, Department of Nano-Medical Science, Graduate School of Medicine, Tohoku University, Seiryo-machi, Aoba-ku, Sendai 980-8575, Japan; e-mail: gonda@med.tohoku.ac.jp.

References

1. Simons M. Angiogenesis: where do we stand now? *Circulation*. 2005;111(12):1556-1566.

2. Carmeliet P. Angiogenesis in life, disease and medicine. *Nature*. 2005;438(7070):932-936.

3. Helisch A, Schaper W. Arteriogenesis: the development and growth of collateral arteries. *Microcirculation*. 2003;10(1):83-97.

4. Simons M, Ware JA. Therapeutic angiogenesis in cardiovascular disease. *Nat Rev Drug Discov.* 2003;2(11):863-871.

5. Gowdak LHW, Poliakova L, Wang XT, et al. Adenovirus-mediated VEGF(121) gene transfer stimulates angiogenesis in normoperfused skeletal muscle and preserves tissue perfusion after induction of ischemia. *Circulation*. 2000;102(5): 565-571.

6. Lu YX, Shansky J, Del Tatto M, Ferland P, Wang XY, Vandenburgh H. Recombinant vascular endothelial growth factor secreted from tissue-engineered bioartificial muscles promotes localized angiogenesis. *Circulation*. 2001;104(5):594-599.

7. Sakr Y. Techniques to assess tissue oxygenation in the clinical setting. *Transfus Apher Sci*. 2010; 43(1):79-94.

8. Gonda K, Watanabe TM, Ohuchi N, Higuchi H. In vivo nano-imaging of membrane dynamics in metastatic tumor cells using quantum dots. *J Biol Chem*. 2010;285(4):2750-2757.

9. Tada H, Higuchi H, Wanatabe TM, Ohuchi N. In vivo real-time tracking of single quantum dots conjugated with monoclonal anti-HER2 antibody in tumors of mice. *Cancer Res*. 2007;67(3):1138-1144.

10. Couffinhal T, Silver M, Zheng LP, Kearney M, Witzenbichler B, Isner JM. Mouse model of angiogenesis. *Am J Pathol*. 1998;152(6):1667-1679.

11. Limbourg A, Korff T, Napp LC, Schaper W, Drexler H, Limbourg FP. Evaluation of postnatal arteriogenesis and angiogenesis in a mouse model of hindlimb ischemia. *Nat Protoc*. 2009;4(12):1737-1748.

12. Hikage M, Gonda K, Takeda M, et al. Nano-imaging of the lymph network structure with quantum dots. *Nanotechnology*. 2010;21:18.

13. Carmeliet P, De Smet F, Loges S, Mazzone M. Branching morphogenesis and antiangiogenesis candidates: tip cells lead the way. *Nat Rev Clin Oncol*. 2009;6(6):315-326.

14. Gerhardt H, Golding M, Fruttiger M, et al. VEGF guides angiogenic sprouting utilizing endothelial tip cell filopodia. *J Cell Biol*. 2003;161(6):1163-1177.

15. Lu EX, Wagner WR, Schellenberger U, et al. Targeted in vivo labeling of receptors for vascular endothelial growth factor: approach to identification of ischemic tissue. *Circulation*. 2003;108(1): 97-103.

16. Tongers J, Roncalli JG, Losordo DW. Therapeutic angiogenesis for critical limb ischemia: microvascular therapies coming of age. *Circulation*. 2008; 118(1):9-16.

17. Jain RK. Normalization of tumor vasculature: an emerging concept in antiangiogenic therapy. *Science*. 2005;307(5706):58-62.

Ultrasonic Coagulation of Large Tissue Region by Generating Multiple Cavitation Clouds in Direction Perpendicular to Ultrasound Propagation

Yuta Inaba, Moriyama Tatsuya, Shin Yoshizawa[*], and Shin-ichiro Umemura[1]

Graduate School of Engineering, Tohoku University, Sendai 980-8579, Japan

[1]*Graduate School of Biomedical Engineering, Tohoku University, Sendai 980-8579, Japan*

High-intensity focused ultrasound (HIFU) therapy is attracting attention as a minimally invasive therapeutic modality. However, it has a problem of a long treatment time. To improve the efficiency of the treatment, we developed a method of coagulating a large region at one time utilizing multiple clouds of cavitation. It is known that acoustic cavitation generated in the focal region of HIFU enhances tissue heating. In this study, cavitation clouds were generated at three positions in the direction perpendicular to ultrasound propagation using high-intensity ultrasound pulses. The tissue in the vicinity of the cavitation clouds was coagulated simultaneously with nonspherically focused ultrasound waves at a relatively low intensity. A high-speed camera was used to observe such behavior of cavitation clouds in a tissue-mimicking gel and to optimize the sequence, and the coagulation performance of the sequence was confirmed with an experiment using excised tissue. The result suggests that the HIFU treatment time is significantly shortened by employing the proposed method. © 2011 The Japan Society of Applied Physics

1. Introduction

In high-intensity focused ultrasound (HIFU) therapy, ultrasound is focused onto a target tissue for coagulation. This method is attracting attention as a noninvasive therapeutic modality. However, it has a problem of long treatment time because cooling time is needed between two consecutive shots of focused ultrasound irradiation to avoid near-field heating due to heat accumulation.[1,2] Therefore, typical HIFU treatment takes 1–3 h.[3–5] To improve its treatment throughput, research studies have been performed to locally enhance ultrasonic absorption using acoustic cavitation, stabilized microbubbles, and their precursors.[6–8] This kind of enhancement is typically effective when assisted by phased arrays because it tends to be transient and therefore needs a fast sequence of irradiation cycles.

Ultrasonically induced cavitation is the primary cause of sonoluminescence and sonochemical reactions and is also known to enhance tissue heating when generated in the focal region of HIFU.[9,10] To improve the efficiency of the treatment, we have been developing a method of coagulating a large region at once by utilizing multiple clouds of acoustic cavitation and named it "triggered HIFU",[11,12] in which an extremely intense focused ultrasound pulse for initiating cavitation[13] (trigger pulse) immediately followed by a moderately intense long-burst focused ultrasound for heating (heating waves) is used.

In our last study, we showed that this triggered HIFU approach can further improve the coagulation throughput by enlarging coagulation volume in the direction parallel to ultrasound propagation.[12] In this study, we show that it can do so in the perpendicular direction even better. Because the energy deposition volume of conventional ultrasonic focusing is much longer in the direction parallel to ultrasound propagation than in the perpendicular direction by one order of magnitude, a much higher heat efficiency is expected for the latter than for the former owing to the smaller surface area of the energy deposition volume. For example, when the energy deposition volume is enlarged by three times, the surface area of the volume for the latter is estimated to be approximately two thirds of that for the former.

To enlarge the power deposition pattern of ultrasonic focusing, a few methods of nonspherical, noncylindrical focusing have been proposed for therapy[14–16] and imaging.[17–19] In this study, time reversal is employed to obtain nonspherically focused heating waves forming an enlarged focus to cover all the cavitation clouds generated by multiple trigger pulses. The cavitation cloud distribution as well as the heating-wave focus may therefore be enlarged in the direction either parallel or perpendicular to the direction of ultrasound propagation.

For reproducible efficiency of this kind of sequence, it is important to ensure whether cavitation clouds can be generated at the intended positions and whether they can survive in an effective form until the heating waves reach there. In this study, a high-speed camera is employed to observe such behavior of cavitation clouds in a tissue-mimicking gel and optimize the sequence. Its coagulation performance is then confirmed in an experiment with excised tissue.

2. Materials and Methods

2.1 Experimental system

Six multifunction generators (NF WF1974) were used to generate and modulate sinusoidal waves at 1 MHz. Synchronization waves at a frequency of 10 MHz were generated with one of the generators and input into the other five generators, whose output waves were input into five RF amplifiers (E&I 100A2), each of which had two pairs of input and output channels, to drive every two of the ten groups of elements of an array transducer. The phase and amplitude can be changed every 100 ns. The 1–3 piezo-composite transducer (Imasonic) had 128 equal area elements, a central frequency of 1.0 MHz, outer and inner diameters of 100 and 36 mm, respectively, and a curvature radius of 100 mm. The 1–3 piezocomposite transducer[20] consists of many small piezoceramic pillars, with a width much smaller than its wavelength, embedded in a polymer filler; each piezoceramic pillar behaves as a point source for forming an acoustic field.[21] Ten transducer elements were electrically combined and connected to either one of the ten amplifiers. The pattern of the connected element groups of the array transducer is shown in Fig. 1. The elements with the same gray level were connected together and numbered

*E-mail address: syoshi@ecei.tohoku.ac.jp